INTERFACIAL INTERACTIONS BETWEEN CARBON NANOPARTICLES
AND CONJUGATED POLYMERS

A Thesis

Presented to the Faculty of California Polytechnic State University

San Luis Obispo

In Partial Fulfillment

of the Requirements for the Degree

Master of Science in Polymers and Coatings Science

by Yanqi Luo

August 2014

COMMITTEE MEMBERSHIP

TITLE: Interfacial Interactions between
                                    Carbon Nanoparticles and
                                    Conjugated Polymers

AUTHOR: Yanqi Luo

DATE SUBMITTED: August 2014

COMMITTEE CHAIR: Shanju Zhang, PhD
                                    Assistant Professor of Chemistry

COMMITTEE MEMBER: Ray Fernando, PhD
                                    Professor of Polymers and Coatings

COMMITTEE MEMBER: John Hagen, PhD
                                    Professor of Chemistry

ABSTRACT

Interfacial Interactions between Carbon Nanoparticles and Conjugated

Polymers

Yanqi Luo

Conjugated polymer based electronics, a type of flexible electronic devices, can be produced from solution by traditional printing and coating processes in a roll-to-roll format such as papers and graphic films. This shows great promise for the emerging energy generation and conversion. The device performance of polymer electronics is largely dependent of crystalline structures and morphology of photoactive layers. However, the solution crystallization kinetics of conjugated polymers in the presence of electron acceptor nanoparticles has not been fully understood yet. In this study, solution crystallization kinetics of poly (3-hexylthiophene) in the presence of carbon nanotubes and graphene oxide has been investigated by using UV-visible absorption spectroscopy and transmission electron microscope. Various kinetics parameters such as crystallization temperature, polymer solution concentration and nanoparticle loading will be discussed. The crystallization rate law and fold surface free energy will be addressed by using polymer crystallization theory of heterogeneous nucleation. This fundamental study will provide a foundation of fabricating high efficiency polymer based electronics.

ACKNOWLEDGMENTS

TABLE OF CONTENTS

LIST OF TABLES

LIST OF FIGURES

1. Introduction

Discovery of conjugated polymers has motivated the field of material engineering and polymer science to fabricate flexible, lightweight and low cost organic electronic devices.[1-3] Due to the low cost solution based process using high throughput roll to roll printing, the conjugated polymer is believed to be one of the best alternative candidates to substitute inorganic semiconductors which are generally fabricated from silicon or gallium.[4] However, these are great challenges to fabricate high performance polymer based devices. In particular, the current challenges are short lifetime and low efficiency of the devices. With intense effort that has been made within the past few decades, for example the power conversion efficiency (PCE) of polymer based organic photovoltaics (POPV) increases but still around 8.0%.[1,2,5]

The essential breakthrough during POPV development is the discovery of photoinduced electro transfer when exited electrons can be transferred from electron donors to electron acceptors. In this case, the photoactive layer processes hybrid structural design containing conjugated polymers as an electron donor and fullerene derivatives as electron acceptors, which is also called bulk heterojunction (BHJ).[5-7] Donor and acceptor molecules are phase separated to form bi-continuous 3-dimensional networks. During this transfer pathway, the band gap alignment of donor and acceptor materials and the interfacial interaction between the two are the determinative factors for charge transfer. Unlike fullerene C_{60} one of the popular electron acceptors, the band gap of carbon nanotubes (CNTs) can be tuned over a wider range by controlling the

diameter and chirality.[8] In addition, the band gap of conjugated polymers is influenced by chemical structures such as bond length, aromaticity and substituents.[1,9] Recently, it has been recognized that interfacial interactions between the conjugated polymer and CNTs are of utmost importance for effectively enhancing the device performance. Even though the interaction between polymers and CNTs in POPV has been well studied, polymer crystal growth kinetics in the presence of CNTs has not been fully understood yet.

In this thesis report, the design of POPV, property of both conjugated polymers and carbon nanoparticles, and polymer crystallization kinetics will be introduced in Chapter 1. Experiment setups, characterization methods, results and discussion of dynamic interfacial interaction study between one of the conjugated polymers poly (3-hexylthiophen) and CNTs and graphene in marginal solvent will be presented in the following chapters.

1.1 Electron Donor: Conjugated Polymers

(a)

(b)

polyacetylene

poly (3-hexylthiophene)
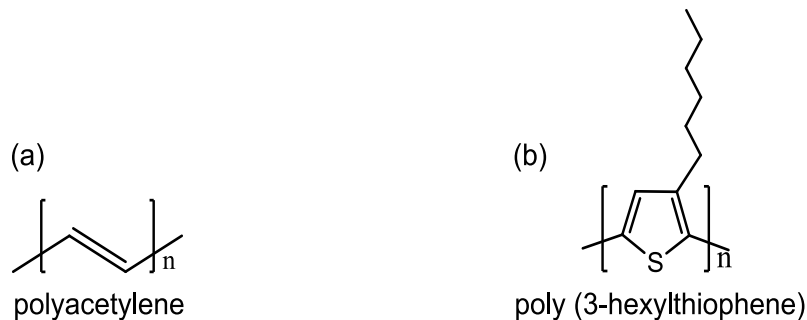
Figure 1. Chemical structures of (a)polyacetylene and (b)poly (3-hexylthiophene)

The first conductive polymer, polyacetylene (CH=CH)$_x$ shown in Figure 1a, was found in 1977 by Shirakawa, Macdiarmid and Heeger,[10,11] whose conductivity can be varied over a wide range by controlling the doping process. Conjugated polymer comprises an alternating single and double carbon-carbon bonds along the polymer backbone. Carbon-carbon single bonds are known as σ-bonds associated with localized electrons. Double bonds consist of one σ-bond and one π-bond whose electrons have higher mobility than σ-bond therefore electron can be delocalized into π-bands over conjugated polymer backbone.[4,10]
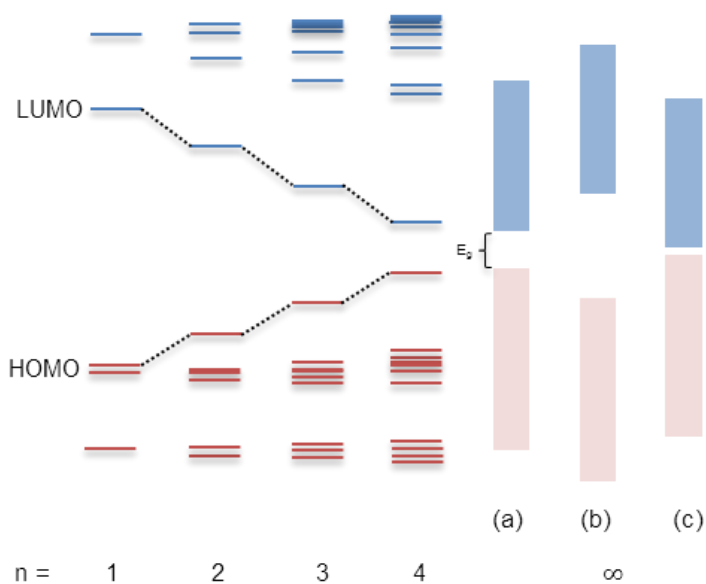
Figure 2. Illustration of polymer band gap. (a) semiconducting polymer (b) insulating polymer (c) conductive polymer

The π-bands have two different bonding in atomic or molecular level: one is where all valance electrons are stable in the ground molecular orbital also referred as highest occupied molecular orbital (HOMO), and the other one is pi

antibonding π^* orbital known as lowest unoccupied molecular orbital (LUMO).[4] In a finite polymer chain, HOMO and LUMO viewed as two distinctive molecular energy bands due to the interaction between repeat units as illustrated in Figure 2,[12] are usually referred to as valance band and conduction band respectively. The energy gap between valance and conduction band defines the actual acquired energy for electron to transit or mobilize from HOMO to LUMO state. Therefore, this energy band gap can be used to divide polymers into these three categories: conductive, semi-conducting and insulating polymers shown in Figure 2. Polymers except conjugated polymers have the nature of being a good insulator due to their large band gaps. Conjugated polymers have typical band gap range from 1 to 4 eV.[12,13] The location of valance and conduction band of conjugated polymers can be significantly altered by doping and changing solvent system.[10]

Polythiophene is a group of conjugated polymer that receives much attention due to its unique combination of efficient electronic conjugation and synthetic versability.[4] Poly (3-alkylthiophene) (P3AT) is one of the polythiophene derivatives. Its polymer chain is made out of π-conjugated polythiophene backbone and pendent alkyl side chains (C_nH_{2n+1}) at 3- position ensuring its solution processability in device fabrication steps.[14] Among P3AT families, regioregular poly (3-hexylthiophene) (P3HT) shown in Figure 1b has been recognized as key materials in organic field effect transistors (OFETs) and organic solar cells (OSCs) due high charge mobility.[15]
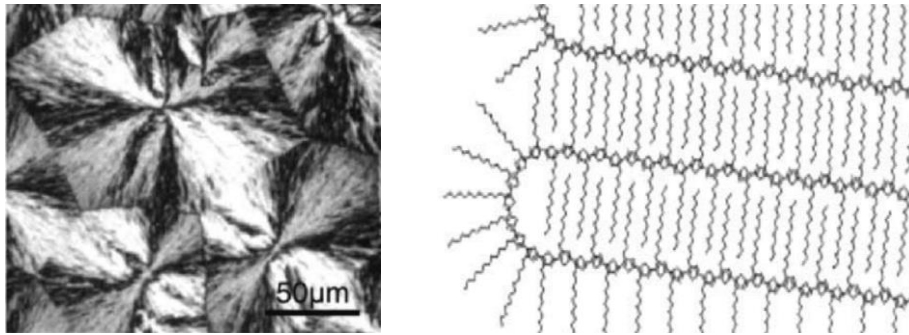
Figure 3. Optical texture spherulites of P3HT and polymer chain packing in spherulites[16]

In flexible semi-crystalline polymers, chain folding is considered as the fundamental basis of lamellar crystal formation. These lamellar crystals can further organize into spherulites (Figure 3) on a large length scale.[17] P3HT is considered as a rigid semi-crystalline polymer since it is comprised of π-conjugated thiophene backbone. However, it has been found that it can be a semi-flexible polymer with persistence length below 3nm in dilute solution.[18] Due to its semi-flexible property and strong $\pi - \pi$ interaction between adjacent polymer backbones, dissolved P3HT polymer chains are capable to fold and form lamellar crystalline domain or even further arrange to spherulites or one-dimensional nanofibrils. Furthermore, using marginal solvents and controlling evaporation rate can significantly modify these nanomorphologies and crystalline domains. Marginal solvents, such as anisole and 1,2,4-trichlorobenzene,

generally have large χ values (Flory interaction parameter) close to or larger than 1.[19] For good solvent such as chloroform, the experiment value of χ is 0.27 for regioregular P3HT.[19] Along with the conformation change from amorphous to semi-crystalline structure, a new absorption peak may appear at a low-energy wavelength.[20] Typically, a solution color change is observed when polymer crystals or aggregates form. Since the formation of polymer crystals is a combination of thermodynamic and kinetic process, this color change is useful to monitor polymer crystals growth.
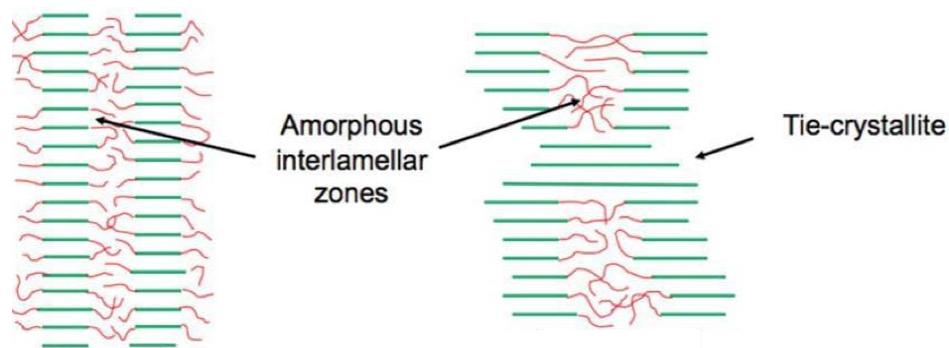
Figure 4. Illustration of conjugated polymer semi-crystalline structures [21]

The conformation and morphology of the polymers is crucial to control the performance in electronic device. Unlike inorganic semiconducting material, charge mobility of the conjugated polymer is profoundly relied upon π-orbital overlap among adjacent chains.[22] π-orbital overlap densities distribute differently over intra- and interchains. Conjugated polymers typically have semi-crystalline regimes containing both amorphous (disordered) and crystalline (ordered) domains as shown in Figure 4. Within the disordered region, excited electrons

are mobilized via hopping (Figure 5a) mechanism with a slower mobility. On the other hand, charge mobility is faster in crystalline domains and improved by a factor of 10 (>0.1 $cm^2V.s^{-1}$) [23] along chain axis due to conduction transport (Figure 5b).
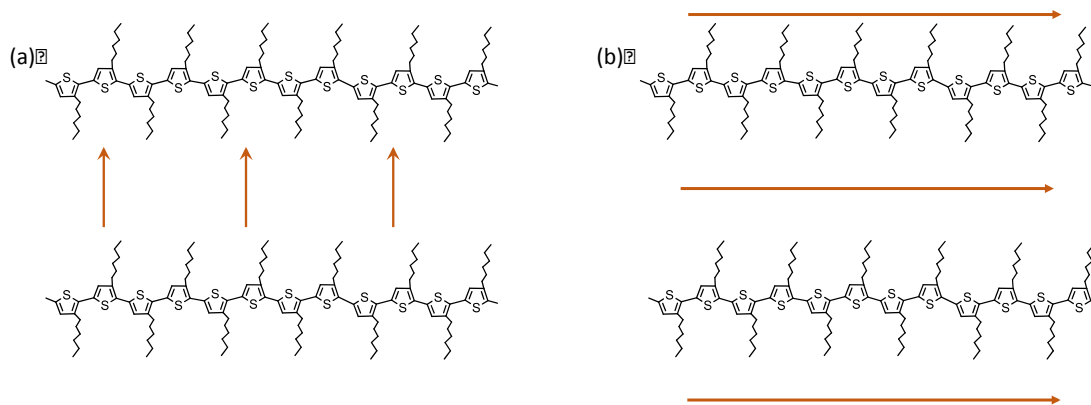
Figure 5. Diagram of hopping and conduction transport

In solution, conjugate polymers such as P3HT can form nanofibrils in marginal solvent due to strong $\pi - \pi$ interaction along polymer backbones. It has been recognized that the existence of P3HT nanofibrils enhances device performance.[9,24] During the formation of polymer nanofibrils, polymer chains experience conformation change from coil to rod and rod-rod aggregation.[25] Recent studies have shown conjugated polymer chains undergo folding during nanofibril formation,[24,26] which have high similarity as traditional flexible semi-crystalline polymers. It is believed that these three steps during conjugated polymer nanofibril formation play different roles in polymer crystal morphology.

To the end, the device performance could be influenced by the polymer crystallization.

1.2 Design Architecture of Organic Solar Cells

Photovoltaic (PV) cells have the functionality of converting solar energy to electricity via photon absorption and electron excitation. Inorganic silicon based and organic polymer based PV cells have distinctive properties and different photoconversion mechanism. Upon light absorption, inorganic based PV directly creates free electron-hole pairs (free charge carriers) which can mobile to $p-n$ junction, while in organic solar cells it leads directly to the production excitons (coulombically bound electron-hole pairs) which dissociate at electron donors and acceptors interface.[27] This occurs due to two reasons mainly: (1) organic materials tend to have a lower dielectric constant compared to inorganic semiconductors, the attractive coulomb potential well between two point charges extends over a larger volume than it does in inorganic semiconductors (Figure 6) and (2) unlike the covalently bounded strong interatomic electronic inorganic semiconducting molecules, organic molecules have weaker non-covalently electronic interactions and therefore electron-hole pairs have the difficulty to separate within the potential well.[27]
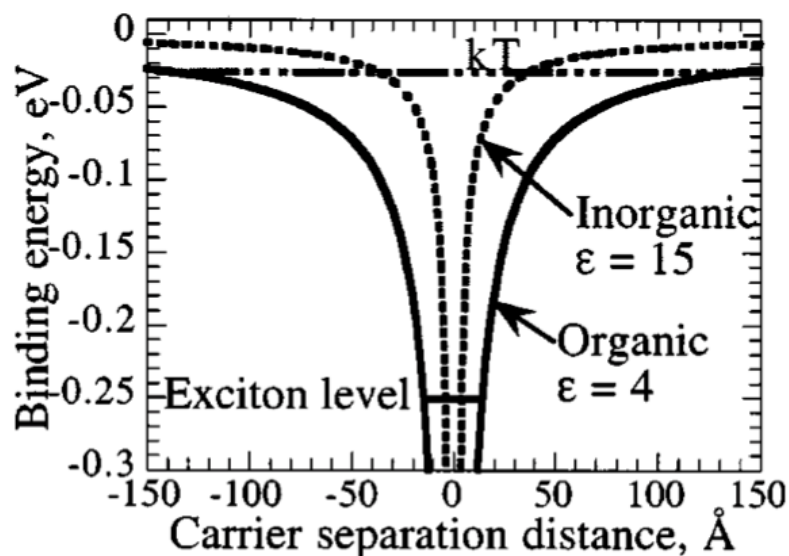
Figure 6. Illustration between binding energy and photogenerated electron-hole pair[27]

Due to the theoretical differences between conventional and excitonic mechanisms, inorganic and organic solar cells have different architecture designs (Figure 7). In most organic solar cells, exciton dissociates at the heterojunction interface into a free electron in one material (electron acceptor) and a hole on other side of interface (electron donor). The effective exciton dissociation is strongly associated with LUMO and HOMO levels in both electron donor and acceptor materials. Generally speaking, electrons on π-conjugated polymer can mobilize relatively easily from HOMO to excited LUMO states when solar energy is acquired. The mobilized electron leaves vacancy in HOMO orbital and this vacancy is known as hole. This coulombically bound electron-hole pair further diffuses from semi-conducting polymers to the surroundings and the probability of exciton dissociates at the heterointerface is high if the length of the

9

domain size of donor and acceptor is consistent with the diffusion length (10-30 nm).[8] Otherwise, excitons recombine themselves and no energy conversion is performed. Once exciton reaches donor and acceptor interface, the excited electron on LUMO state is relaxed to LUMO level of electron acceptor when the energy gradient is the slightly higher than the charge transfer (CT) energy state where electrons and holes are separated but not released from columbic attraction.[28] Recently, it has been found that Type II heterojunction (staggered band gap of polythiophene and carbon nanotubes), where HOMO of electron donor is higher than HOMO of electron acceptor but lower than LUMO of electron acceptor, provides the most effective exciton dissociation (Figure 8) among the other types of energy band gap alignment.[29]
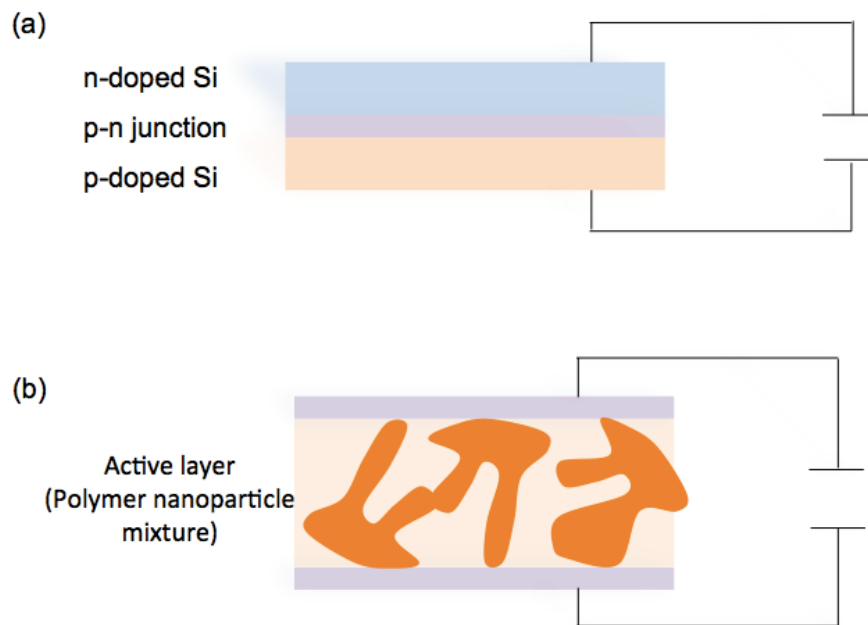
Figure 7. Architecture designs of conventional and organic solar cells

Unlike planar silicon $p - n$ junction photovoltaic solar cells, heterojunction structure is more favorable in organic solar cells to provide larger interfaces within the photoactive layer. This aspect requires a good interfacial interaction between donor and acceptor materials. Semi-conducting nanoparticles are the most promising acceptors material due to the large surface areas, which will be further introduced in Chapter 1.3. Currently, the most efficient polymer-based PV cells to date uses one of fullerene derivatives ((6,6)-phenyl-C_{61}-butyric acid methyl ester, PCBM) as electron acceptor with approximately 7% PCE.[9]
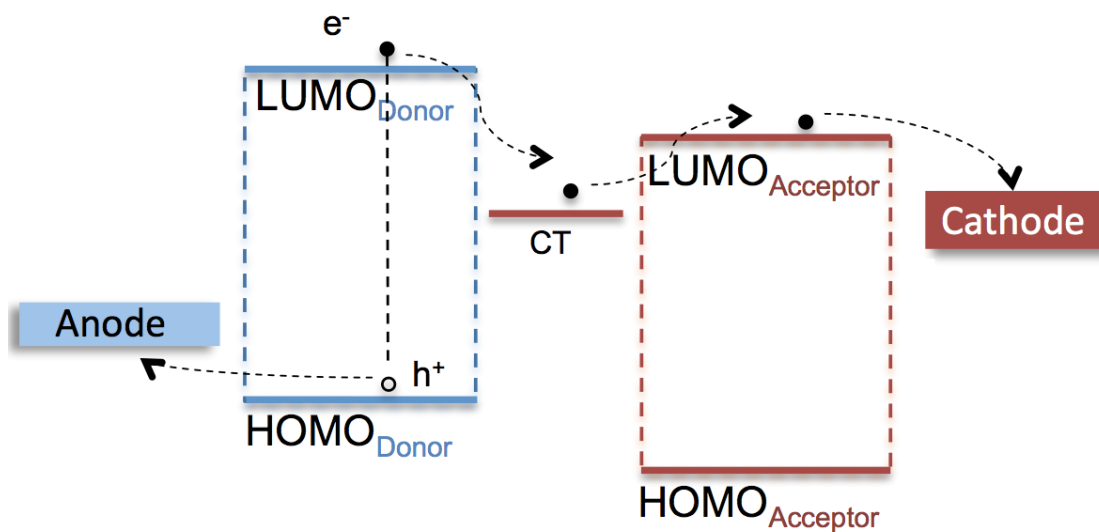
Figure 8. Exciton Dissociation Scheme at Heterointerface

1.3 Electron Acceptor: Carbon Nanoparticles

Even though fullerene derivatives exhibit the best performance among bulk heterojunction PV, its PCE is still far less than 23.2% of the theoretical limit.[30] Fullerenes are fully conjugated and closed-cage molecules containing hexagonal and pentagonal faces. C_{60} is the most abundant and stable member

within the family and it is commonly chemically functionalized to produce methanofullerene, PCBM (Figure 9). High concentration PCBM is needed to enhance device performance due to its spherical geometry structure.[4] However, when a system consists of a large amount carbonaceous, the result of solar energy is below optimal because PCBM is favorable in absorbing Ultra-Visible wavelength energy. Furthermore, the presence of relatively high concentration of fullerene derivatives prevents semi-conducting polymer from forming large lamellar crystalline domains leading to decline charge mobility within polymeric matrix.

(a)   (b)
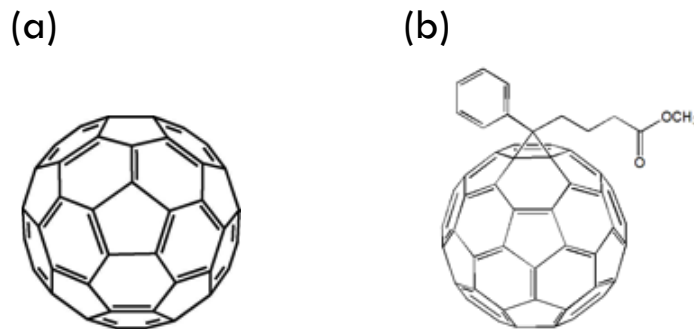
Figure 9. Chemical structure of (a)C_{60} fullerene and (b)PCBM [3]

1.3.1 Carbon Nanotubes (CNTs)

To enhance PCE of PV devices, it has been suggested to replace fullerene derivatives by carbon nanotubes (CNTs).[4,8,28,31,32] The CNTs are a one-dimensional (1-D) nanostructured allotropic form of carbon. Energy conversion efficiency can be improved by introducing CNTs due to the ballistic conduction pathway. Ballistic conduction pathway is commonly observed when electrons do

not scatter within the medium. According to quantum electrodynamics, electrons can be scattered by either charged particles through electrostatic interaction or any electromagnetic field. The scattered electrons have a moving direction that deviates from original ones resulting in a shorter moving distance or shorter mean free path. Besides longer mean free path, CNTs also provide a tunable band gap that can be tailored toward any desire PV systems by controlling the diameter and chirality.[33]

Despite such great potential, polymer PV cells using CNTs as electron acceptor materials have shown limited device performance, and its PCE is typically below 1.0%.[4,8] [28] Only recently, the dramatic improvement has been achieved in boron-doped CNTs with 4.1% PCE.[34] It has been recognized that the presence of metallic CNTs (m-CNTs) is the dominant limiting factor in device performance because m-CNTs enhance electron-hole recombination.[35] m-CNTs and semi-conducting CNTs (s-CNTs) are coexisting during CNTs synthesis and the amount of m-CNTs is close to one third for a typical CNTs synthesis[9]. The band gap different between m-CNTs and s-CNTs is the result of chirality. Using single-walled carbon nanotubes (SWNTs) as an example, the formation of it can be pictured as a sheet of graphene rolled into a cylindrical shape. Chiral vector define the rolling direction and angle, which is expressed as two indices (*n*, *m*) shown in Figure 10. The band gap of CNTs can vary from 0 to 2eV due to the chirality difference.[33,36] During the past years, intense efforts have been made toward ultra-purification of CNTs, and full separation of semiconducting and

metallic CNTs.[37] Centrifugation has been considered as one of the effective way to separate s-CNTs and m-CNTs due to the density variation between the two.
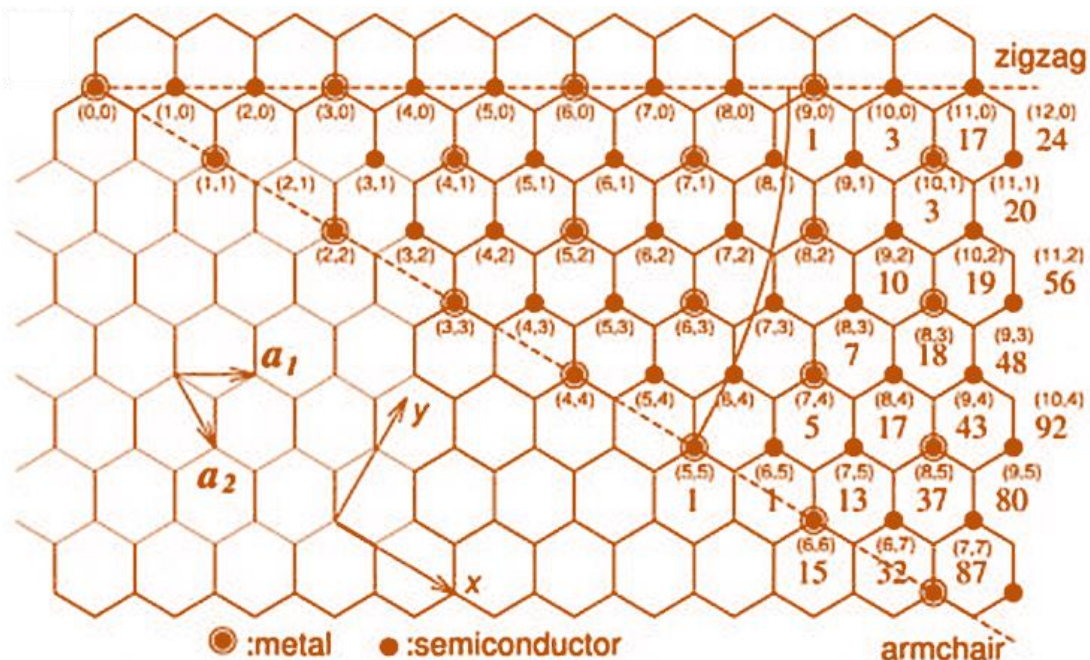
Figure 10. Types of SWNTs mapped on graphene sheet [9]

Besides chirality effects, another challenge to incorporate CNTs into PV cells is the solubility and nanotube bundle formation.[9,26,38] Unfunctionalized CNTs normally have low solubility in most organic solvents; and the sp^2 hybridize hexagonal carbon ring resulting in strong Van der Waals intermolecular interaction between adjacent tubes, which makes CNTs easily form bundles or aggregates. The best way to solve this issue is to attach different chemical functional groups on the sidewalls or surfaces of CNTs. The presence of attached functional groups not only act as dispersion stabilizers but also perform as bundle exfoliate agents. The successful attachment can be achieved via either

chemical functionalization or noncovalent wrapping technique.[9,39-41] In chemical functionalization, the linkages between functional groups and CNTs surfaces are covalently bonded. The benefit of this covalent approach is that the linkage is mechanically stable; therefore a longer stable CNTs dispersion is obtained. However, this chemical covalent approach is least favorable in device fabrication because the destruction of chemical hybridization and the disrupted mechanical properties have been observed with the additional covalent linkage.[42]

On the other hand, preserving optical, electrical and mechanical properties of CNTs via noncovalent wrapping approach is more preferred even though the intermolecular interaction between sidewalls of CNTs and the wrapping agent is not permanently stable over time. Semiconducting polymers happen to be a good wrapping agent as a consequence of strong $\pi - \pi$ stacking interaction due to the similarity of their conjugated backbones and sp^2 hybridized nanotube sidewalls. Classical molecular dynamic simulation predicts that at equilibrium state the conjugated backbones have a tendency to align themselves along the long axis of CNTs to maximum $\pi - \pi$ stacking, resulting in an elongated conjugation length and also a fast interfacial electron transfer.[41,43-45] Conjugated polymer has shown a strong intermolecular interaction with CNTs interface experimentally. Various kinetically trapped polymer conformations have been observed using high-resolution imaging tools such as transmission electron microscope (TEM), including metastable circumstance and helix structures (Figure 11).[39,40] Diameter of nanotubes is the main factor that dictates the helix structure of conformationally restricted conjugated polymer and CNTs blends.
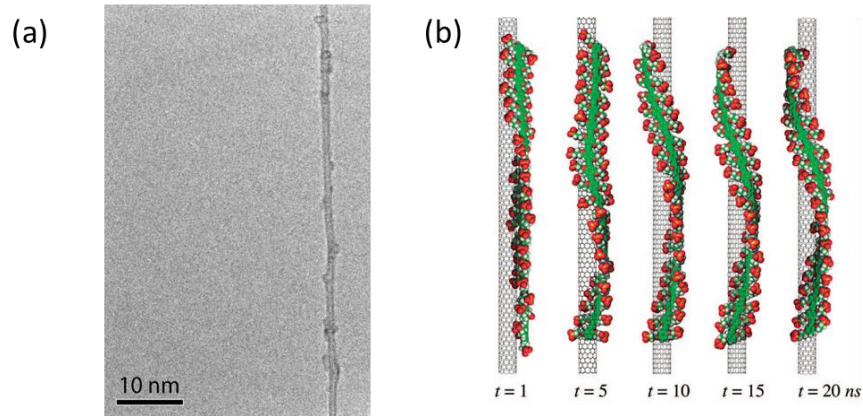
Figure 11. (a) TEM Image of Polymer Helix Structures on SWNTs and (b) Helix wrapping simulation [26,27]

Although conjugate polymers are originally practiced as a wrapping agent, it has been recently recognized that CNTs serve as an orientation template to organize conjugated polymers in an ordered pattern at the interface.[24,46] In addition, the CNTs can also act as heterogeneous nucleation agent for polymer crystallization.[47-49] The CNTs induced polymer crystallization provides two advantages: increase nanotubes solution processability and improve performance of PV solar cells.

1.3.2 Graphene

Graphene has received extensive interest because of its high electron mobility, good conductivity and elasticity. Graphene is a two-dimensional structural material, comprised of a monolayer honeycomb-like hexagonal sp^2 hybrdized carbon atoms. [50,51] Since CNTs can be considered as a rolled graphene nanosheet, these two nanomaterials are expected to have very similar

mechanical, electrical and thermal properties but with a different surface area and surface energy. Some research groups have found that mixing a very small amount of graphene sheets in polymer matrices can enhance electrical and thermal properties by a significant amount.[28] Reduced Graphene oxide (rGO) is a similar material as graphene but can be an inexpensive substitute for graphene. The monolayer graphene sheet is usually obtained from chemical vapor deposition (CVD) or any deposition method. However, synthesize the precursor of graphene, graphene oxide, from graphite powder is an alternative approach to inexpensively produce graphene with high throughput. The chemical reactions to convert graphite to graphene are the simple oxidation reactions. However, one disadvantage of this wet synthesis is the introduction of defects on graphene nanosheeets.
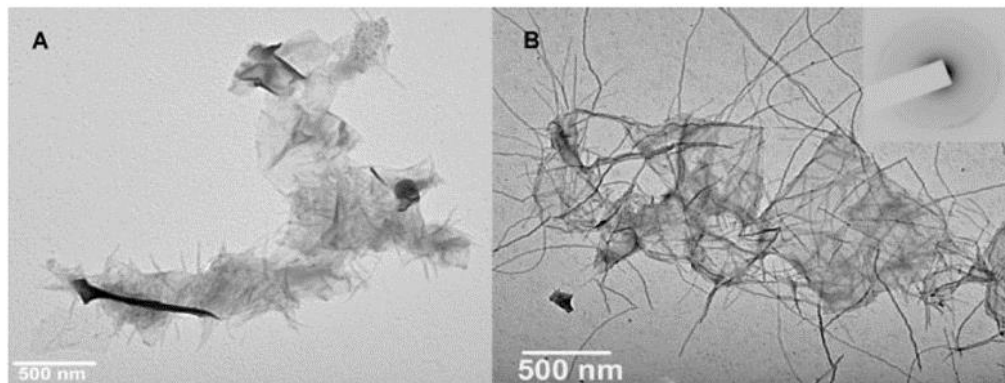
Figure 12. TEM images of a) rGO/P3HT with short polymer nanowires b) P3HT nanofibrils structure on rGO formed in solution [52]

Recently, several groups demonstrate the possibility of reduced graphene oxide (rGO) induced the formation of P3HT nanofibrils (Figure 12). [52-54] This

implies that reduced graphene oxide has the potential to be used as an electron acceptor in organic PV cells, particularly with the formation of P3HT nanowires and supramolecular structure, and large surface area compared to CNTs.

1.4 Semi-Conducting Polymer Crystallization

Unlike small molecules, polymer crystallization process is rather complex and has not been fully understood yet especially for conjugated polymer. Small molecules crystallization, from vapor, the melt or solution is controlled by both homogenous (primary) nucleation and crystal growth (secondary nucleation) on an existing crystal surface.[55] Two different models are used to describe nucleation rate i. The first model derived from Boltzmann's law is dominated by two opposing factors: the free energy of nuclei formation (ΔG_n) and free energy of deposition (ΔG_η):[55]

$$i = \left(\frac{NkT}{h}\right) exp\left[-\frac{(\Delta G_n + \Delta G_\eta)}{kT}\right] \qquad (1.1)$$

where N is the number of uncrystallized elements, k is the Boltzmann constant and T is the constant temperature. In the model, molecules crystallization process is controlled by nucleation on a smooth surface. The second crystallization model, well known as continuous growth model, suggests that crystal growth rate is directly proportional to temperature gradient ΔT ($\Delta T = T_m - T_c$, where T_m is equilibrium melting temperature and T_c is crystallization temperature) on a rough surface. Both models are useful for analyzing small

molecule single crystal formation process. However, to study polymer crystallization besides thermodynamic parameters, inter- and intra- chain interaction, and crystallinity degree, are the uncontrollable parameters that contribute the biggest challenges. Conjugated polymers, different from traditional polymers such as polyethylene, are more rigid and have strong inter- and intra-$\pi - \pi$ interaction. Currently, no perfect model has been used to describe their crystallization process but the idea of three-step, coil to rod transition, polymer chain folding, and rod-rod aggregation,[25,48] polymer crystal formation has been recognized (Figure 13). In this work, we borrow the basic thermodynamic rate law and two other useful models, Avrami and Hoffman-Lauritzen theories, from traditional polymer to investigate the formation process of P3HT crystals.

The concept of S-shape of the general transformation-time curve, which describes when a new phase establishes at rate first slow, second fast and finally in equilibrium, has been accepted. Avrami model has been widely used to investigate phase transition of materials in solution or the melt crystallization and this model implies that phase transition occurs is the consequence of tiny "ultra nuclei" from existing crystals along with geometry change under isothermal condition.[56] Avrami model is only valid under isothermal condition because the number of effective nuclei is proportional to given temperature. Avrami theory is established with the second assumption, which is the rate of volume growth of the crystal is proportional to its surface area.[56] Avrami model can be described as:

$$1 - X_t = \exp(-kt^n) \qquad (1.2)$$

Where n is Avrami exponent that describes the geometry structure of nuclei, k is the Avrami crystallization rate and X_t is the relative crystallinity at time t. In this work, Avrami model is used to evaluate the reaction mechanism of pure P3HT solution crystallization and SWNTs induced P3HT crystallization. Since reaction mechanism is strongly associated with nuclei shape and crystal geometry, it is meaningful to apply natural logarithm transform on Avrami model (Eq 1.2) as shown in Eq 1.3.

$$\ln[-ln(1-X_t)] = \ln k + n \ln t \qquad (1.3)$$

From this form, the Avrami exponent can be obtained as the slope of the function of $\ln[-ln(1-X_t)]$ versus natural logarithm of time t. When distribution of effective nucleation site is not random, Avrami exponent n is an integer value in the range of 1 to 3.[56] Rod-like nucleating geometry is present when n is 1; platelets nucleating site is present when n is 2; and sphere nucleating site when n is 3.
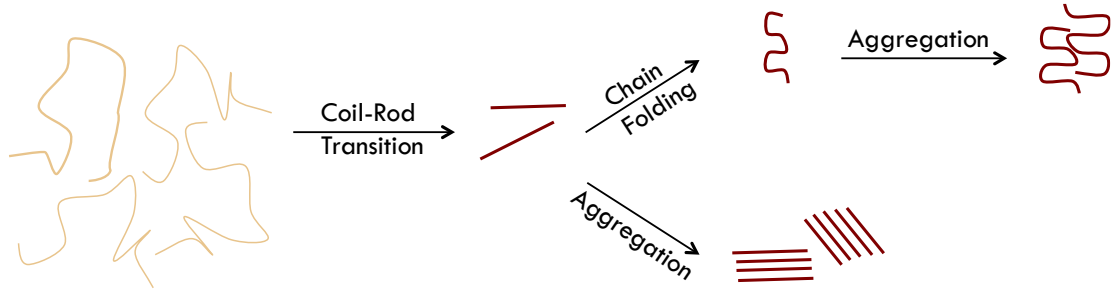
Figure 13. Illustration of conformational transition of polymer chains from random coil to crystals

Since growth rate G is independent to seed size under isothermal condition, it can be viewed as a function of polymer concentration as shown in Eq 1.4.[57]

$$G = kC^{\alpha} \qquad (1.4)$$

Where C is polymer concentration, k is reaction constant and α is reaction order. Like Avrami exponent, reaction order is controlled by reaction mechanism. For example, reaction order for elementary or single step reaction is based on stoichiometry. However, since polymer crystallization process is complex and it involves three different steps as shown in Figure 13, the overall reaction order is reasonable to evaluate by combining the reaction mechanism from each step. The crystallization process starts with the transition from random coil amorphous polymer chain to straightened rod-like state. The rod-like polymer chains can either form rod-rod aggregates or experience polymer chain fold based on polymer concentration and polymer chain length. The folded polymers can further aggregate due to strong interactions. According to nucleation theory, growth rate G is linearly proportional to nucleation rate S. The overall nucleation rate can be expressed as:[58]

$$S_{overall} = w_{fold}S_{fold} + w_{coil}S_{coil} + w_{aggregate}S_{aggregate} \qquad (1.5)$$

where w_i is the weight factor of each steps but this value is extremely difficult to precisely determine. However, it has been found that S_{fold} is proportional to the concentration raised to a power less than unity, $S_{aggregate}$ is raised to the second power,[58] whereas S_{coil} is raised to an inverse first-order according to recent

experimental data.[25] Based on the interpretation of nucleation rate at different steps, the overall reaction can be viewed as the sum of the exponential factor from individual step.

The last model that is used to further understand solution crystallization mechanism of conjugated polymer is Hoffman-Lauritzen (HL) secondary nucleation theory. In fact, this secondary nucleation theory is the first analytical model to assess the conversion of three-dimensional (3-D) random coil conformations to chain folded ordered lamellar crystals.[55] HL theory is one of the most comprehensive and widely used model to interpret the behavior of polymer chains in crystallization kinetics.[59] From thermodynamic consideration, the consequence of conformational transition of random coil amorphous chains to ordered lamella crystals is to minimize Gibbs free energy with smaller entropy value when temperature is below the melting point of polymers. According to HL theory, the deposition of the first stem has two steps as shown in Figure 14. The process starts with polymer chains in melt (random coil state, Figure 14a) which try to align short sections of molecules (black dots in Figure 14b) with the depositing substrate. The alignment process involves chain elongation and stretching along the depositing substrate. After many attempts of stretching and elongating, at a point in time, the individual aligned sections (activated complex) contribute to a full stem on the substrate (Figure 14c).[60]
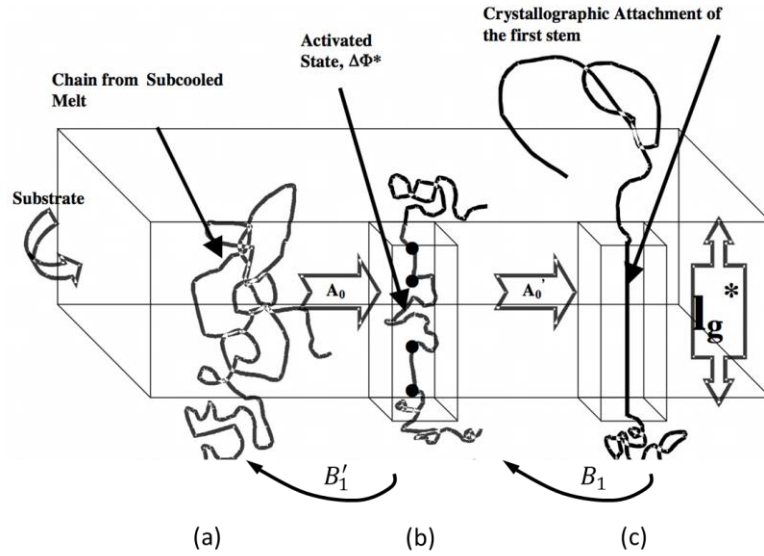
Figure 14. Formation of initial deposition stem on substrate[59]
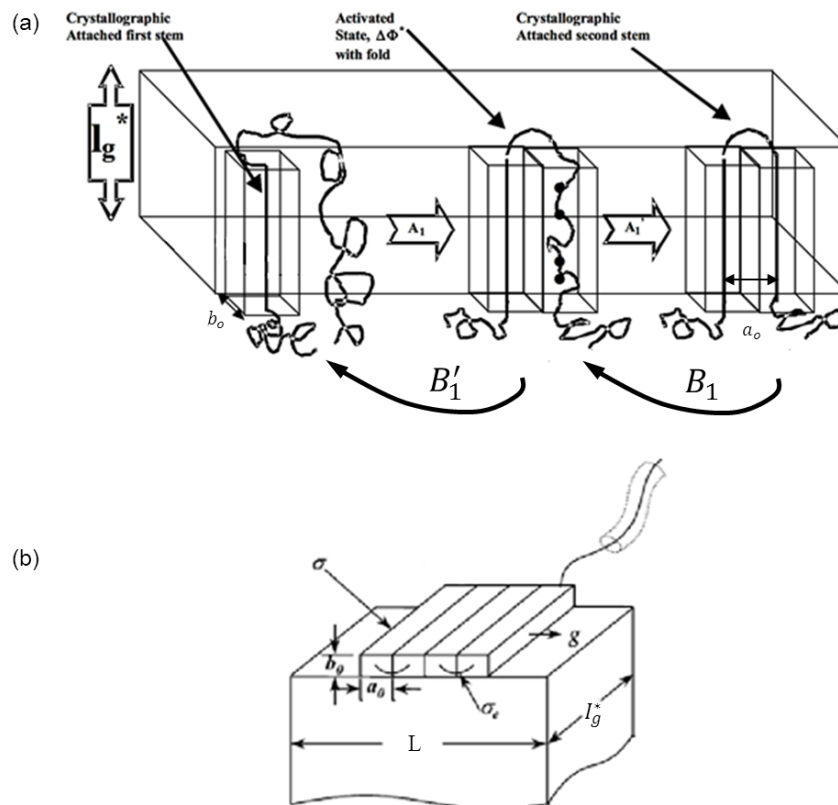
Figure 15. Schematic illustrations of second attached stem.[59] (a) Side view (b)

Top view

The formation of activated complex with a rate constant A_0, a slower process than the crystallographic attachment step with a rate constant A_o', is the rate-determining step during first stem deposition. The whole stem deposition process also accompanies with the backward reaction (removal of the first stem) with rate constants B_1 and B_1'. The other important aspect of first stem deposition is the creation of two additional lateral surfaces with work being equal to $2b_o\sigma l$, where b_o is lamellar layer thickness, l is length of chain attached and σ is lateral surface free energy. In reality, l is not a fix value especially when the substrate is not smooth. Thus, an average value l_g^* is used in HL nucleation model. Once the first stem is deposited, the remaining polymer chain experiences chain fold and forms ordered lamellar crystal continuously as shown in Figure 15. The parameter σ_e, fold surface free energy, is introduced in mathematical expression of the following stem deposition due to polymers chain fold mechanism; and a_o is the width or spacing between two aligned stems.
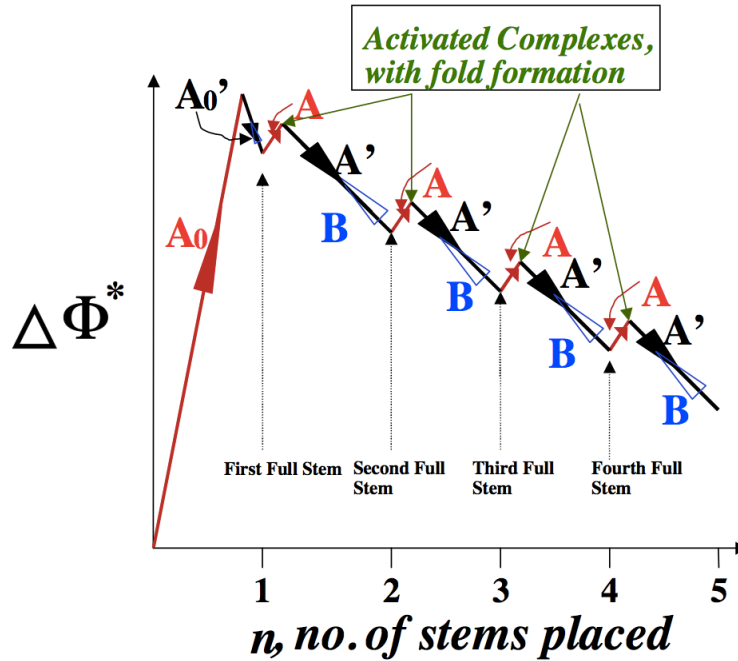
Figure 16. Illustration of falling activation energy in lamella crystal formation[59]

The energy barrier $\Delta\phi^*$ for first stem deposition is the largest among crystal lamellar formation. This energy barrier, activation energy of stem deposition, of subsequence polymer chain is illustrated in Figure 16 where *A* is the rate constant of polymer chain fold and *B* is for the backward reaction. Based on the steady state flux calculation, the rate of stem deposition *S* is expressed as:

$$S = \frac{N_o A_o (A-B)}{A-B+B_1} \tag{1.6}$$

where N_o is the number of initial stems and the rate constants are experssed as:

$$A_o = \beta' e^{\frac{-2b_o l\sigma + \psi' a_o b_o l \Delta G_f}{kT_c}} \tag{1.7}$$

$$A = \beta e^{\frac{-2b_o l\sigma_e + \psi a_o b_o l\Delta G_f}{kT_c}} \tag{1.8}$$

$$B_1 = \beta' e^{\frac{-(1-\psi')a_o b_o l\Delta G_f}{kT_c}} \tag{1.9}$$

$$B = \beta e^{\frac{-(1-\psi)a_o b_o l\Delta G_f}{kT_c}} \tag{1.10}$$

where k is Boltzmann's constant, T_c is crystallization temperature and ΔG_f is the free energy of crystal formation. β and ψ are pre-exponential factor and apportionment factor respectively. Initial stem and subsequence stem depositions are believed to have different β and ψ value due to the variation in attachment motion. Thus, β' and ψ' are used to represent the subseqence deposition steps; β and ψ are for the initial stem deposition. However, traditional HL model assumes $\psi' = \psi$ and $\beta' = \beta$ because it's extremely challenge to measure these factors in solution. The value of ψ is in a range of 0 to 1, and the mathemetically expression of β is shown in Eq 1.11

$$\beta = J e^{\frac{-U^*}{R(T_c - T_\infty)}} \tag{1.11}$$

and

$$J = \frac{\kappa}{n}\left(\frac{kT_c}{h}\right) \tag{1.12}$$

where U^* is activation energy of deposition, R is ideal gas constant, T_∞ is equal to glass transition $T_g - 30$ and another pre-exponential factor J. J is a frequency

factor representing events per second. n is the number of repeat units of polymer and κ is the monomeric friction coefficient.[60]

The overall growth rate G of polymer crystals is contributed from two important parameters, the surface nucleation rate i and the substrate completion rate g. The mathematically surface nucleation rate is shown in Eq 1.13, where l_u is the monomer length and n_l is the number of stems of width a_o that make up the substrate of length L.[60]

$$i = \frac{1}{l_u n_l a_0} \int_{\frac{2\sigma_e}{\Delta G}}^{\infty} S(l)dl \qquad (1.13)$$

The substrate completion rate is given by:[60]

$$g = a_o(A - B) \qquad (1.14)$$

After substituing Eq 1.6 to 1.10 into Eq 1.13 and 1.14, i and g are expressd below.

$$i = \frac{N_o\beta}{n_l a_o l_u}\left[\frac{kT}{2b_o\sigma} - \frac{kT}{2b_o\sigma + \Delta G_f}\right]exp\left[\frac{-4b_o\sigma_e\sigma}{\Delta G_f kT_c}\right] \qquad (1.15)$$

$$g = a_o\beta\left[1 - \exp\left(\frac{a_o b_o \delta l \Delta G_f}{kT_c}\right)\right]exp\left[\frac{-2a_o b_o\sigma_e}{kT_c}\right] \qquad (1.16)$$

During polymer crystallization process, the competition between surface nucleation rate and substrate completion rate may result in three different regimes as predicted in HL nucleation theory shown in Figure 17. In Regime I when $i \ll g$, the growth front is quickly covered by one lateral crystal nucleus

before any new nuclei are laid down.[59] The mathematical equation for the growth rate in regime I is given by:[55]

$$G_I = ib_oL \qquad (1.17)$$

In Regime II when $i \approx g$, more than one nuclei are allowed to form on the surface. The mathematical expression of Regime I is modified to accurately describe the relationship between growth rate and other kinetics parameter shown as:

$$G_{II} = (ib_og)^{1/2} \qquad (1.18)$$

This analytical expression implies that the growth rate of the regime II is independent of the width of substrate surface. In Regime III when $i \gg g$, large amount of nucleation events undergo and little or no substrate completion takes place. The analytical model of the regime III is expressed as below:

$$G_{III} = ib_oL' \qquad (1.19)$$

After substituting i and g expression (Eq 1.15 and 1.16) into Eq 1.17-1.19, the overall growth rate of polymer crystals G in three different regimes are:

$$G_I = G_{0I}exp\left(\frac{-U^*}{R(T_c-T_\infty)}\right)exp\left(\frac{-K_{gI}}{T_c\Delta T}\right) \qquad (1.20a)$$

$$G_{II} = G_{0II}exp\left(\frac{-U^*}{R(T_c-T_\infty)}\right)exp\left(\frac{-K_{gII}}{T_c\Delta T}\right) \qquad (1.20b)$$

$$G_{III} = G_{0III} \, exp\left(\frac{-U^*}{R(T_c - T_\infty)}\right) exp\left(\frac{-K_{gIII}}{T_c \Delta T}\right) \qquad \text{(1.20c)}$$

Where,

$$G_{0i} = \frac{N_o b_o J}{l_u}\left[\frac{kT_c}{b_o \sigma} - \frac{kT_c}{2b_o \sigma + a_o b_o \Delta G_f}\right] \qquad \text{(1.21)}$$

$$K_{gI} = K_{gII} = 2K_{gIII} = \frac{4b\sigma\sigma_e T_d^0}{k_B \Delta H_f} \qquad \text{(1.22)}$$

ΔT is the degree of supercooling which is measured from the equilibrium dissolution temperature T_d^0 (where $\Delta T = T_d^0 - T_c$), and K_g is the nucleation parameter which is a function of the fold surface free energy and lateral surface energy. HL theory is applied in this work to evaluate and calculate the fold surface free energy of P3HT during solution crystallization process once K_g is obtained by plotting lnG against $\frac{1}{T_c \Delta T}$.
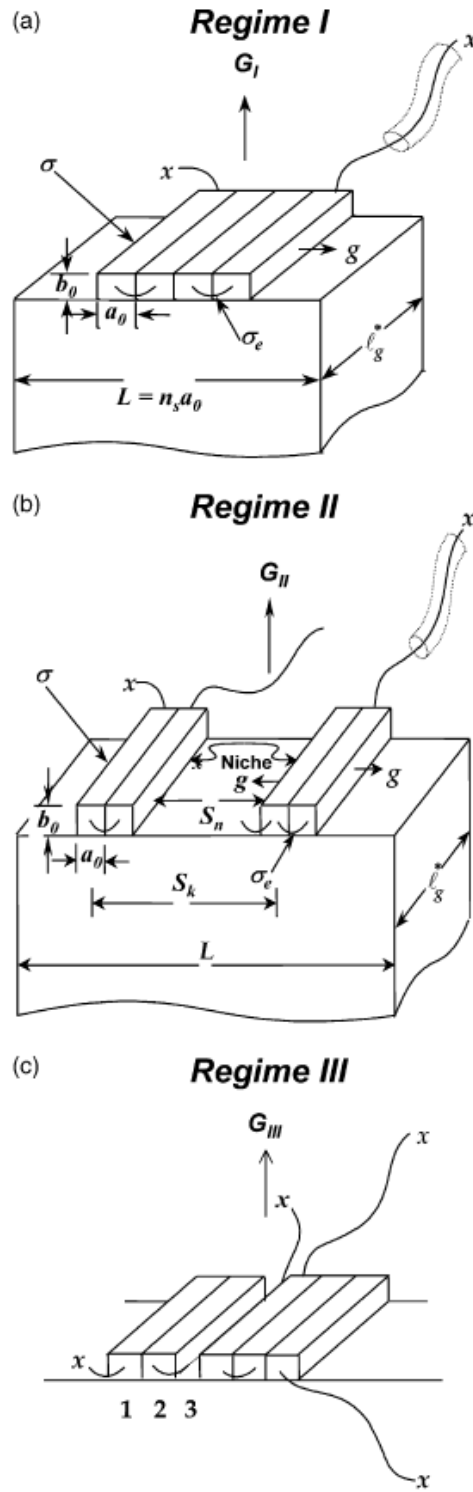
Figure 17. Diagrams of three regimes from HL theory [55]

2. Experimental and Methods

All materials that were used in this thesis work were purchased from commercially available sources by Zhang's Research Group. Graphene oxide was synthesized using the modified Hummers' method.[61] Natural graphite flake powders were used as the starting material, which were exfoliated under acid and thermal treatment. The exfoliated graphite interlayers were oxidized to produce graphene oxide aqueous-gel like material. Ultraviolet-visible (UV-vis) absorption spectroscopy was the main quantitative instrument for measuring the formation of SWNTs induced crystal of semi-conducting polymers poly (3-hexylthiophene).

2.1 Materials

Regioregular (91-94% head-to-tail) Poly (3-hexylthiophene – 2,5-diyl) (P3HT, average M_w = 50,000 – 70,000, Rieke Metals), single-walled carbon nanotubes (SWNTs) (99 wt% purity, Cheap Tubes Inc), anisole (99% pure, Acros Organics), 1,2-dichlorobenzene (DCB, 99% extra pure, Acros Organics) were purchased from commercially available sources and used without further purification.

2.1.1 Single-Walled Carbon Nanotubes Dispersion

SWNTs (0.625 mg) and P3HT (1.25 mg) were added to DCB (5 mL) in a 20 mL glass vial with a 1:2 ratio. The mixture was ultrasonically agitated for two hours in a water bath at 25 °C and the glass vial was labeled as SWNTs stock

solution with [SWNTs] = 0.125 mg/mL. A micropipette was used to transfer this SWNTs stock solution (400 µL) to another glass vial that had (1600 µL) DCB in order to prepared a further diluted SWNTs dispersion for SWNTs induced P3HT solution crystallization kinetics study.

2.1.2 P3HT Solution Preparation and Formation of P3HT Nanofibrils

A 1.25 mg/mL stock solution of P3HT in anisole was prepared in a hot oil bath at 80 °C and then diluted into different concentration solutions for the study of crystallization kinetics. P3HT nanofibrils can be formed with or without addition of prepared SWNTs dispersion. Formation of P3HT nanofibrils occurred when transferring hot P3HT solution at 80 °C to any desirable isothermal crystallization temperature T_c. The range of T_c varies due to the solubility of crystalline P3HT in different solvent. Typically, the P3HT solution was mixed with a certain amount of SWNTs dispersion at 80 °C for at least 5 minutes to erase thermal history of the sample, when studying the SWNTs induced effects on P3HT crystal growth, and then the mixture was quickly cooled at approximately 180 °C/min to the preset isothermal T_c.

2.1.3 Graphene Oxide Synthesis and Dispersion Preparation

Flake graphite powder (1.0 g) was added to a mixed acid solution of H_2SO_4 (30.0 mL) and HNO_3 (10.0 mL) with a 3:1 volume ratio in 100 mL round bottom flask under ice bath while stirring. Once the addition was completed, the ice bath was removed and the graphite acid mixture was allowed to stir for 24 hours. The mixture was then transferred to 200 mL water in a beaker dropwise

via a glass pipette. This acid treated graphite was collected via vacuum filtration and was washed using water until the pH was 5. After drying at 60 °C for another 24 hours, the graphite intercalated compounds (GICs) were obtained.

The dry GIC powder was added to the same mixed acid solution as the previous acid treatment in a 100 mL round bottom flask and the mixture was ultrasonically agitated for three hours. A paste like mixture was obtained indicated GICs exfoliation. The exfoliated GICs were collected via vacuum filtration. The collected solids and H_2SO_4 (200.0 mL) were mixed and stirred in a 250 mL round bottom flask in an ice bath. Then, $KMnO_4$ (10.0 g) was added to mixture dropwise while keeping mixture temperature below 20 °C. The ice bath was removed and the round bottom flask was placed in an oil bath at 35 °C for three days until the mixture became viscous and changed to a brown reddish color.

The mixture was transferred to an ice bath and DI water (200.0 mL) was added to the mixture to quench the oxidization reaction under stirring for 30 minutes. H_2O_2 (3.0 mL) was poured slowly under stirring to the mixture for 30 minutes. A phase separation was observed after allowing the mixture to settle for one hour. The top layer that contained the residual permanganate ions was in purple color; and the bottom layer contained graphene oxide was in yellow slurry like suspension. The suspension was washed with HCl (2.0 mL) to remove any residual ions and acids from oxidation. The graphene oxide was further washed with DI water until pH reached 5 and the gel like graphene oxide was collected via ultra-centrifugation.

2.2 Characterization Methods

2.2.1 Transmission Electron Microscope

Transmission electron microscope (TEM) images were collected on an EFI Tecnai G2 sphera microscope at an accelerating voltage of 120kV. TEM uses a high-energy electron beam transmitted through a thin sample. The interaction between electrons and thin film matter can develop a relatively higher resolution images. Therefore, TEM images can be used to characterize and analyze the microstructure of materials within atomic scale resolution. Typically, interfacial interaction between P3HT and carbon nanoparticles or surface morphology of P3TH polymer itself can be visually illustrated in TEM images. The TEM samples were prepared by drop-casting the diluted solution of P3HT and SWNTs to the holey carbon film on 300 mesh copper grids. The samples were examined without staining or shadowing under TEM.

2.2.2 UV-visible Absorption Spectroscopy

The UV-Vis absorption spectra were received in solutions on a Jasco V-550 UV-Vis spectrophotometer equipped with temperature-control and magnetic stirring features. The sample chamber was insulated from surroundings during the data collection. Absorption spectroscopy is employed as an analytical chemistry tool to quantitatively determine the concentration of a particular compound only if the matter can interact with electromagnetic radiation.

In UV-vis absorption spectroscopy, the valance electron of an atom or a molecule is promoted from lower energy level or ground state to a higher energy level or excited state with the absorption of photons energy. The energy different between occupied molecular orbitals (σ, π bonds and non-bonding orbital n) and unoccupied molecular orbitals (sigma antibonding σ^* and pi antibonding π^*) corresponds to ultraviolet and visible radiation. Therefore, it is possible to use UV-visible absorption spectroscopy to detect organic molecules or polyatomic ions.[62] Table 1 summarizes the possible electronic transition involving different molecular orbitals.

Table 1. Electronic transition and wavelength range involving $\boldsymbol{\sigma}$, $\boldsymbol{\pi}$ and $\boldsymbol{n}$ molecular orbitals [62]

Transition	Wavelength Range	Examples
$\sigma \rightarrow \sigma^*$	< 200 nm	C-C, C-H
$n \rightarrow \sigma^*$	160 – 260 nm	H_2O, CH_3OH, CH_3Cl
$\pi \rightarrow \pi^*$	200 – 500 nm	C=C, C=O, C=N, C≡C
$n \rightarrow \pi^*$	250 – 600 nm	C=O, C=N, N=N, N=O

Absorbance is the signal that UV-visible spectroscopy measures. Intensity of absorbance is determined by logarithm of the amount of photons transmitted through sample against the amount of photons emitted from light source, which can be rewritten as:

$$A = -log\frac{P_T}{P_0} \qquad (2.2)$$

Ultraviolet-visible absorption spectroscopy is one of the great analytical instruments for kinetic study of P3HT crystallization process since amorphous and crystalline P3HT have distinctive interaction with photons. When majority P3HT polymer chains are in a random coil state, the polymer solution has λ_{max} at 450 nm. However, crystalline P3HT λ_{max} was redshifted to 600 nm due to thermochromism.

3. Results and Discussion

3.1 Solvent Effect on P3HT Nanofibrils Formation
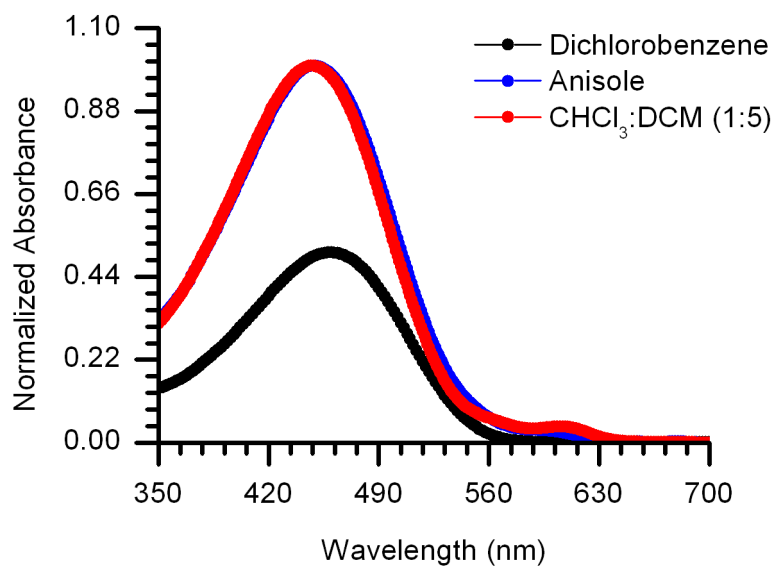
Figure 18. Solvent effects on P3HT solution crystallization in ambient

environment

The Solvent system is a very crucial condition to study P3HT crystal formation in solution under ambient environment. In this regard, different solvent systems are used to investigate P3HT crystallization process. This solvatochromism analysis is accomplished by using UV-vis spectroscopy. Three different solvent-systems are used and compared. They are anisole, dichlorobenzene (DCB), and a 2-solvent system composed on chloroform and dichloromethane (DCM) in 1:5 ratio. In this context, the definition of good or poor solvent is defined based on polymer-solvent interaction. In a good solvent, most polymer chains have strong interaction with solvent resulting in random coil

conformation evidenced by the maximum absorbance at wavelength 450nm.[25] On the other hand, in poor solvent, polymer chains start to form rod-like conformation then aggregate demonstrated by the maximum absorbance at wavelength 600nm.[20] As shown in Figure 18, the effects of solvent on P3HT crystallization process can be easily conducted by evaluating the normalized absorbance value at 600nm. In DCB solvent system, the absorbance at this low energy wavelength is close to zero. This implies almost no rod conformation of P3HT is detected. The other two solvent systems, anisole and chloroform-DCB, on Figure 18 indicates the formation of rod-like P3HT crystal. In this thesis work, anisole is selected to be the solvent system.

3.2 Interfacial Morphology

We employed transmission electron microscope (TEM) to directly visualize interfacial morphology and structures of P3HT on SWNT surfaces after the complete solution crystallization. Figure 19a and 19b shows typical bright-field images of the ordered P3HT nanofibril crystals grown in anisole in the presence of SWNTs at room temperature. This is the evidence that P3HT polymer chain can form crystalline nanofibrils with an approximately 20nm diameter perpendicularly oriented to the long axis of SWNTs. This nanofibril structures, hybrid shish-kebab, have been widely seen and studied in CNT-induced polymer crystallization.[42,47,63-65] This observation is also consistent with recent report on P3HT-SWNT nanofibrils.[65] The length of P3HT nanofibrils and the attachment density on nanotube surfaces are highly dependent on crystallization temperature, nanotube loading against polymer concentration, and molecular

weight of the polymer. The long axis of the crystalline nanofibrils corresponds to the direction of $\pi - \pi$ stacking, which implies conjugated backbone is aligned parallel to the long axis of SWNTs (Figure 19c).[14,65] The resulting ordered nanofibrils representing efficient interfacial electron transfer and fast exciton dissociation. Experimental research has shown that polymer PV solar cells with an active layer containing ordered P3HT-SWNT nanofibrils have demonstrated much improvement on device performance.[66]
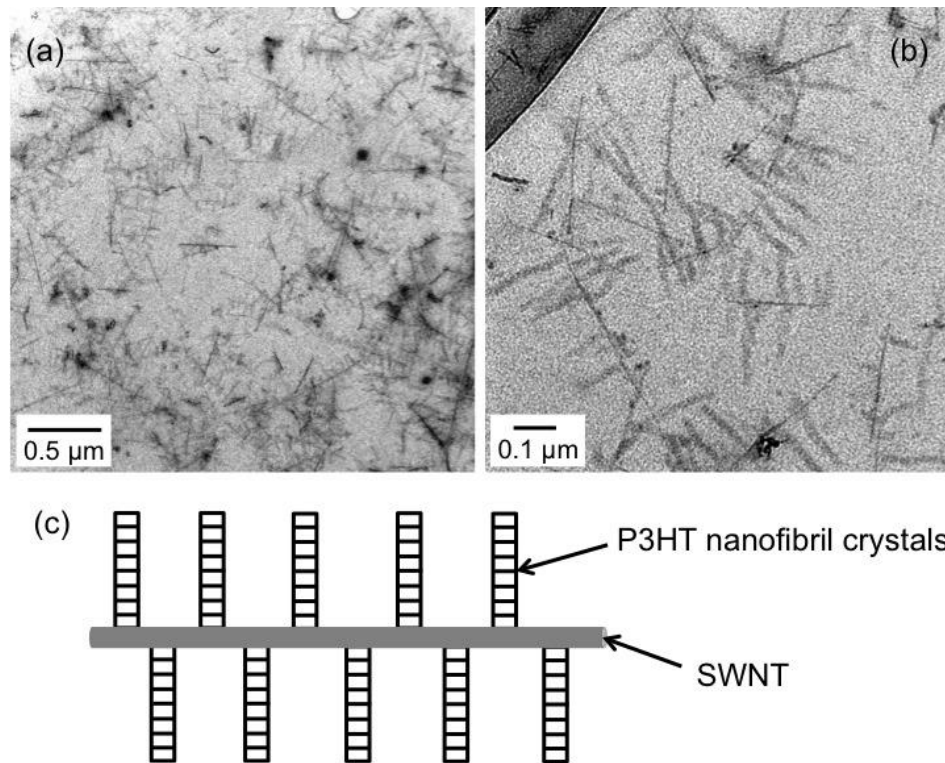
Figure 19. (a) and (b) Bright-field TEM images of P3HT nanofibril crystals in the presence of SWNTs. (c) Schematic diagram of P3HT nanofibril crystals perpendicular to the long axis of SWNTs.

3.3 Solution Crystallization Kinetics
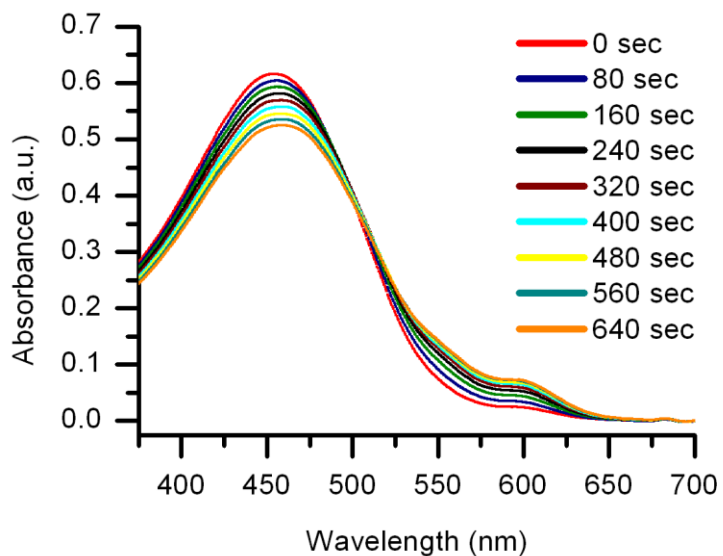
Figure 20. Time-dependent chromism of P3HT in anisole at 298K. Concentration of P3HT is 0.020 mg/mL

The kinetics of SWNTs induced P3HT solution crystallization in anisole has been successfully studied using *in situ* UV-visible spectroscopy. The solution crystallization kinetics of pristine P3HT in anisole has also been investigated under the same conditions as a reference shown on Figure 20 and 21; there are time dependent chromism and effect of polymer concentration on isothermal solution crystallization process of P3HT respectively.
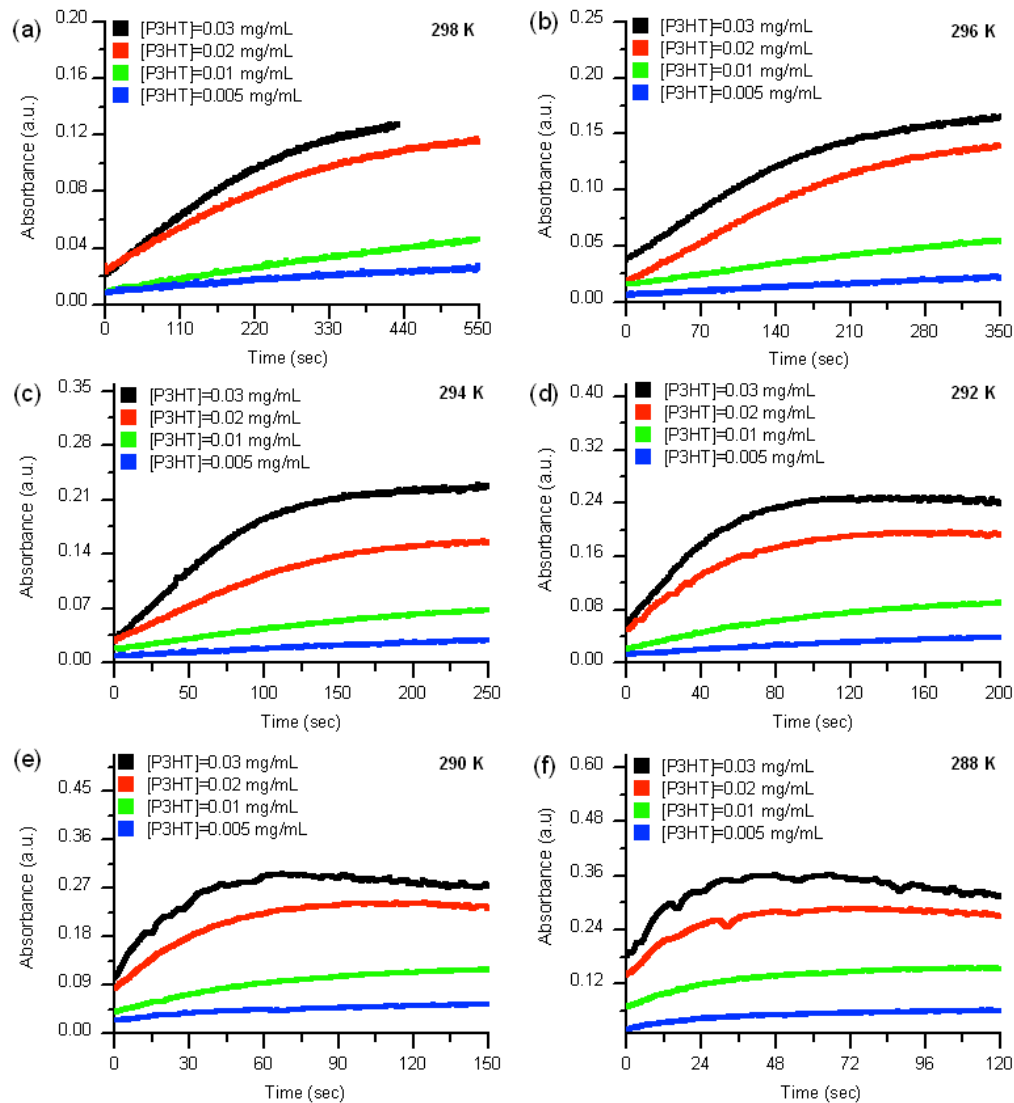
Figure 21. Solution crystallization kinetics of P3HT at different crystallization temperature and with different polymer concentrations. The absorbance value is obtained at 600 nm

To determine the appropriate isothermal crystallization temperature (T_c), a set of temperature dependent absorbance measurement has been performed on P3HT in anisole containing 0.10 wt% SWNTs as shown in Figure 22a. At high

temperature of 323K, P3HT solution exhibits an absorption maximum at λ = 450nm, suggesting the coil-like conformation of the dissolved polymer chains.[25] With decreasing thermal energy, the absorbance at λ = 450nm decrease significantly while low energy absorption bands at λ = 560nm and λ = 600nm appear and their absorption signal gradually increase. Both new vibronic bands are contributed from rod-like conformation and electronic interaction in P3HT crystals.[67] The presence of a distinct isobestic point at λ = 480nm further suggests the coil to rod transition during polymer solution crystallization. Since absorbance at λ = 600nm has a directly linear relationship with P3HT crystallinity in solution,[20] the crystallization process of SWNTs induced P3HT can be monitored by using the absorbance at this fixed wavelength.

In this work, crystallization temperature is carefully chosen in the range from 292K to 323K. This T_c window selected from the cooling curve on Figure 22b, where at ~323K absorbance starts to gradually increase till 292K. Although solution crystallization process continuously undergoes beyond 292K, time response delay between instrument and actual coil to rod transition has been observed. Thus, 292K is an appropriate lowest T_c in this study. It should be noted that this thermochromism process of P3HT solution containing SWNTs is reversible with the presence of rate-dependent hysteresis. The cooling and heating curves correspond to the crystallization and dissolution process, respectively. Therefore, the dissolution temperature (T_d) during solution heating can be measured via UV-vis spectroscopy.
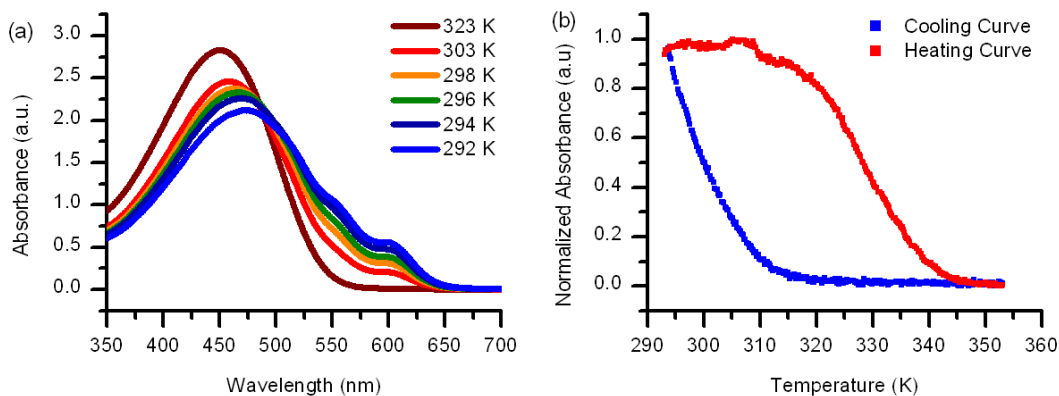
Figure 22. (a) Thermochromism of P3HT with 0.10 wt% SWNTs in anisole and (b) heating (red) and cooling (blue) curves of absorbance at $\lambda = 600$nm versus temperature. P3HT concentration is 0.020 mg/mL, and heating and cooling rates in (b) are 2.0 K/min.
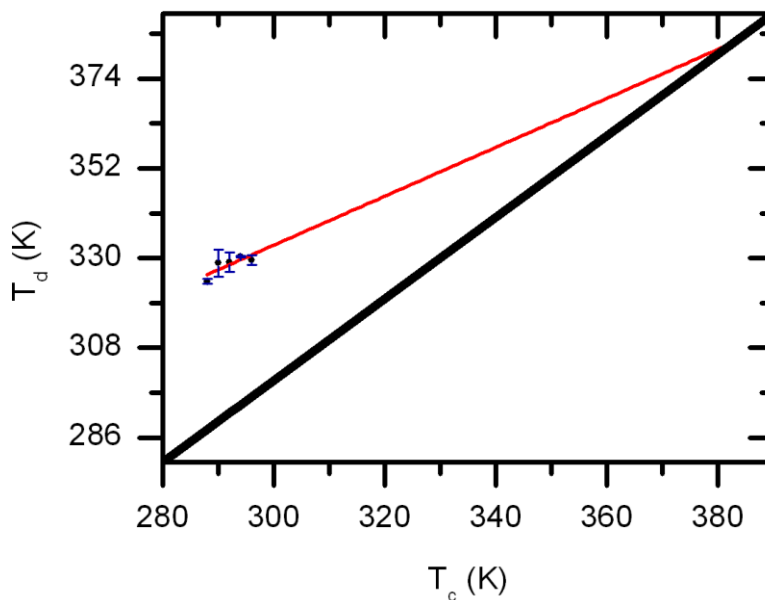
Figure 23. Dissolution Temperature (T_d) of P3HT in anisole as a function of isothermal crystallization temperature (T_c). The data is linearly extrapolated to the line of $T_d = T_c$ to obtain T_d° at the intersection point. The concentration of P3HT is 0.020 mg/mL.
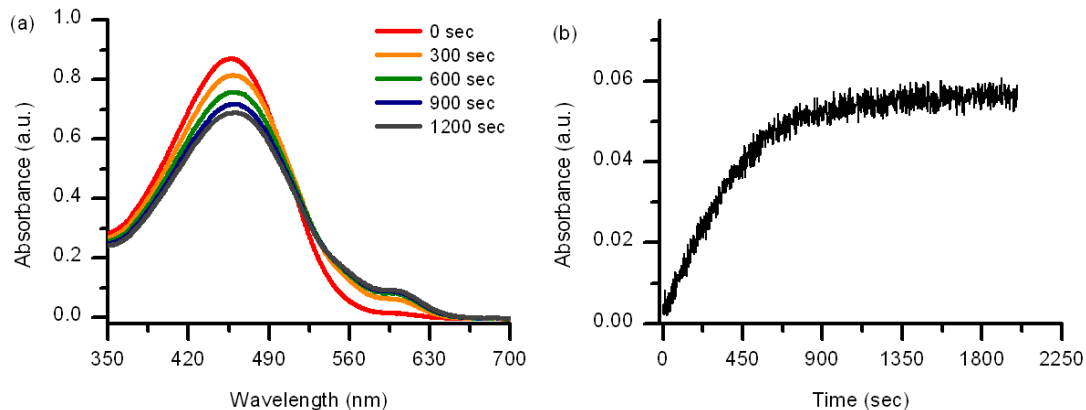
Figure 24. (a) Time-dependent chromism of P3HT with 0.10wt% SWNTs in anisole at 298K and (b) Absorbance at $\lambda = 600$nm versus crystallization time. The concentration of P3HT is 0.010mg/mL.

Hoffman-Weeks method was applied to evaluate the dissociation temperature at equilibrium (T_d°) of pristine P3HT in anisole.[60] Once reached the completion of isothermal crystallization process at the preset crystallization temperature (T_c), P3HT samples were heated up to the temperature that dissolves the produced crystals. Both crystallization and dissolution process were monitored by UV-vis. Once T_d is obtained after analysis UV-vis spectrum under dissolution process, the data were plotted as T_d versus Tc as shown in Figure 23. The diagonal line in Figure 22 represents the function of $T_d = T_c$. The data set T_d versus T_c was then extrapolated linearly to the diagonal line, which produced an intersection T_d°. In this work, the value of T_d° of the control P3HT in anisole was calculated to be ~ 381 ± 10K. This value is consistent with 371K of the recent

literature report on P3HT crystallization in anisole.[48] The large uncertainty value is expected due to narrow T_c window.[57]

Similar to Figure 20, Figure 24a illustrates time-dependent chromism of P3HT with 0.10 wt% SWNTs upon cooling the hot solution from 353K to 298K. With the aging time from 0 to 1200 sec, the absorbance at λ = 450nm decreases while the absorbance at λ = 600nm steadily increases, indicating SWNT-induced crystallization of P3HT in anisole. The crystallization process was further evaluated by *in situ* studying the absorbance at λ = 600nm over time as shown in Figure 24b. It also displays the differential growth of P3HT crystals decrease over time with decreasing slope of absorbance versus time. The growth rate reaches a plateau when the dissolved polymer is exhausted. Figure 25 shows the absorbance at λ = 600nm over time plots of solution crystallization of P3HT in anisole with various SWNTs loading under different crystallization temperature (T_c). The method of initial rates was use to evaluate and study the growth rate of polymer crystallization kinetic behavior.[25] In this method, the initial slope of absorbance versus time plots was extracted. The initial growth rate data is further summarized and plotted in Figure 26. As thermodynamic theory predicted, decreasing crystallization temperature results in the coil-to-rod transition to minimized total free energy and then, accelerates the crystallization process of P3HT. When isothermal condition is applied, addition of SWNTs to P3HT solution obviously increases the growth rate as shown in Figure 26 as well. This phenomenon can be easily explained by considering nucleation and chain growth process. SWNTs promoted crystallization behavior suggests that SWNTs act as

a heterogeneous nucleating agent effectively for P3HT crystallization. The growth rate increases more or less proportionally with addition of SWNTs loading.
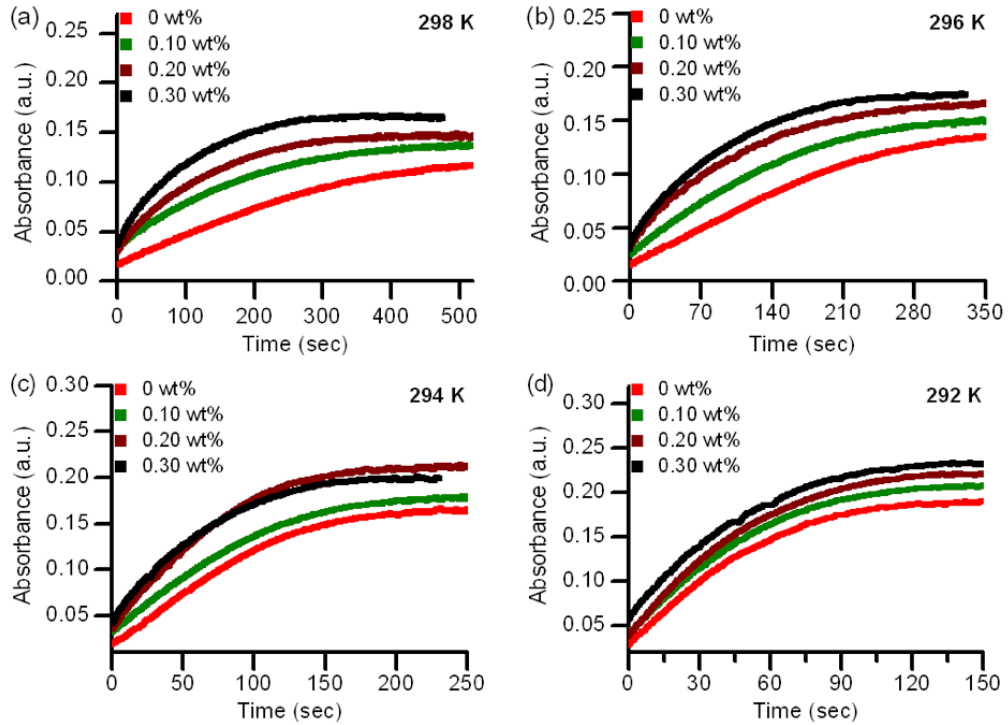
Figure 25. Kinetics of isothermal solution crystallization of P3HT with various loading of SWNTs at different crystallization temperature. (a) 298K, (b) 296K, (c) 294K and (d) 292K. Concentration of P3HT is 0.020mg/mL

Theoretically, the concentration (*C*) dependence of the growth rate (*G*) at constant temperature is expressed by equation below:

$$G = kC^{\alpha} \tag{3.1}$$

where k represents the rate constant and α is the reaction order. The latter term, α, is only associated with reaction mechanism. To validate the reaction mechanism, the equation needs to be transformed to natural logarithm:

$$lnG = \alpha lnC + lnk \qquad (3.2)$$
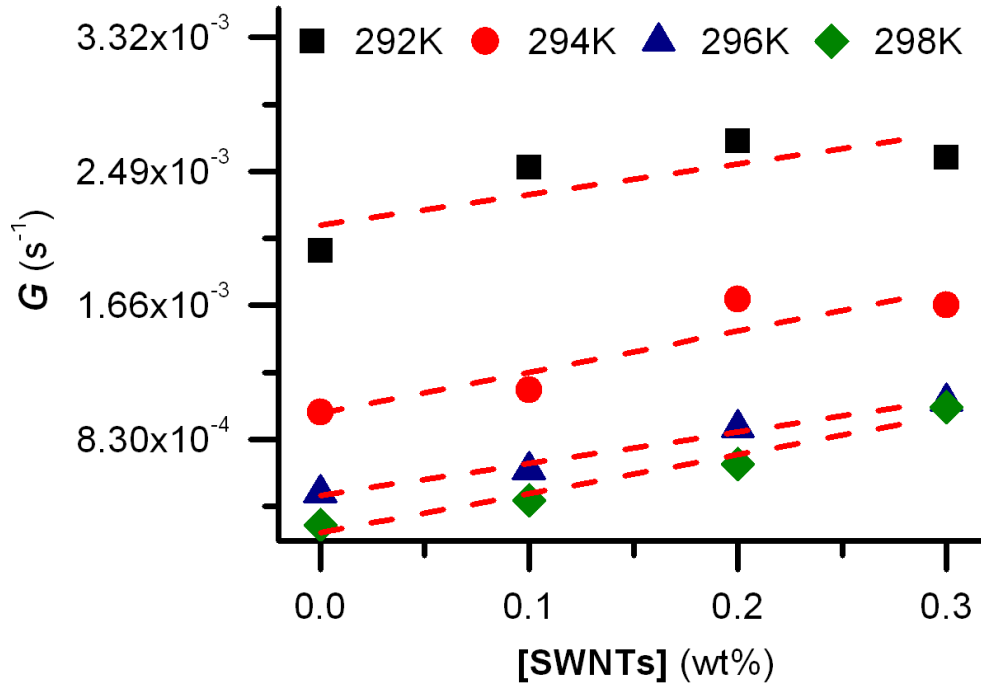
Figure 26. Effect of SWNT loading on the growth rate of P3HT crystals in anisole. Concentration of P3HT is 0.020 mg/mL.

The plots of *lnG* against *lnC* were obtained as shown in Figure 27. The data points of the control P3HT and P3HT-SWNTs fall onto the best fit straight lines and the slopes of the straight lines are the reaction order α. The reaction order for each different SWNT loading is summarized in Table 2. It is found that α

is fall in the range from 1.5 ~ 1.7 for the control and 1.6 ~ 1.8 for P3HT-SWNTs. This data indicates that the addition of SWNTs does not change reaction mechanism. Based on secondary nucleation theory, the rod-rod aggregation has predominant influence over the coil-rod transition and chain-folding during solution crystallization of P3HT.[65] Thus, the slightly increase in value of reaction order α with the presence of SWNTs may reflect strong rod-rod aggregations due to the template effect SWNTs.
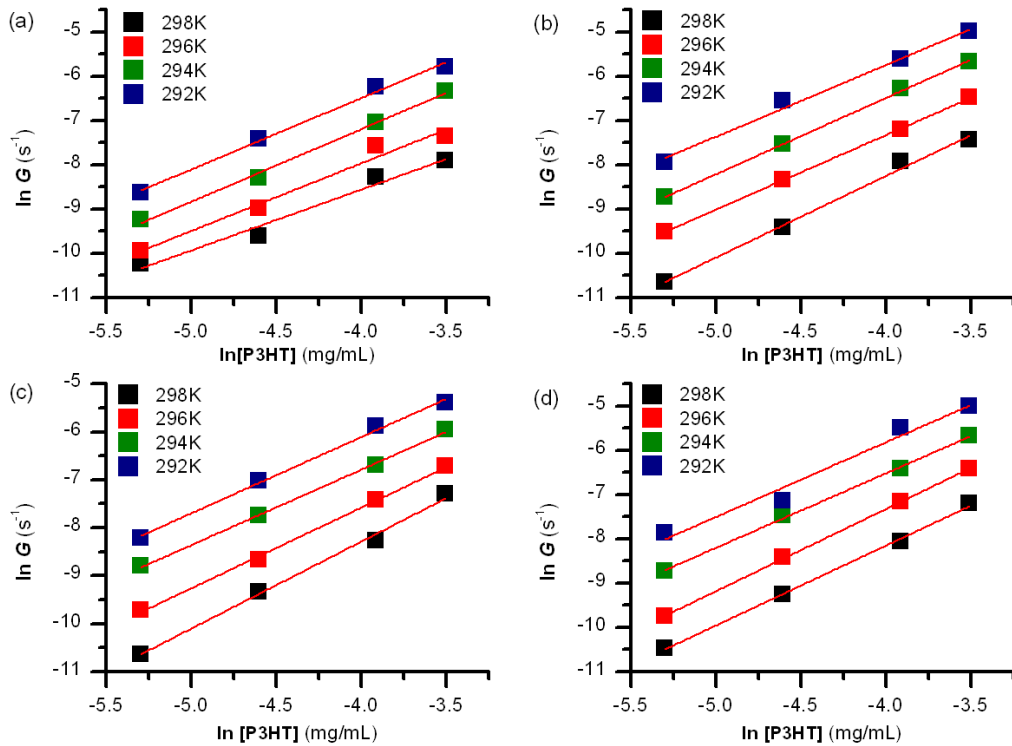
Figure 27. Plots of ln G versus ln [P3HT] at different crystallization temperature for P3HT with various loading of SWNTs. (a) control P3HT (b) 0.10wt%, (c) 0.20 wt% and (d) 0.30 wt%.

3.4 Nanotube Nucleation

The growth rate of the crystals (G) is proportional to the nucleation rate (S) as $G \propto S$ based on polymer crystallization theory.[58] To clearly explain the nucleation geometry and nature growth of the nuclei, the classical Avrami theory is applied as shown below:[2]

$$1 - X_t = \exp(-kt^n) \tag{3.3}$$

As the crystallinity is linearly related to the UV-Vis absorbance at $\lambda = 600\text{nm}$,[20] the value of X_t is determined by:

$$X_t = \frac{A_t - A_0}{A_{max} - A_0} \tag{3.4}$$

where A_0, A_{max} and A_t are, respectively, the initial absorbance, the maximum absorbance and the absorbance at time t. To simplify the Avrami model, the double logarithmic linear form is obtained as shown:

$$\ln[-ln(1 - X_t)] = \ln k + n \ln t \tag{3.5}$$

Figure 28 shows the plots of ln[-ln(1-X_t)] versus ln t for control P3HT and P3HT with various loading of SWNTs at different temperature. Most of the experimental data fall onto the best fit straight lines; only at high relative crystallinity, the data slightly deviate from the straight lines, indicative of the existence of secondary crystallization.[68] The values of the Avrami exponent n and the Avrami rate constant k were then calculated from the slope and intercept of the straight lines, respectively. The data is also summarized in Table 2. Our results show that the value of Avrami exponent n vary from 1.10 to 1.31 for the pristine P3HT and from

1.01 to 1.27 for P3HT-SWNTs. This result is well consistent with the literature report on isothermal melt crystallization of conjugated polymers P3HT with n in a range of 0.6 to 1.4 indicating a rod-like nucleating sites.[69,70] Furthermore, the solution crystallization process of P3HT in anisole is in one-dimensional (1-D) nucleation and with the present of SWNTs does not change polymer crystallization process since the variation between the two Avrami exponents is small. The slight decrease in the value of the Avrami exponent *n* by adding SWNTs is attributed to geometric confinement of polymer chains at the interface due to the orientation template effect of SWNTs. At constant SWNT loading, the value of Avrami exponent *n* is sensitive to the crystallization temperature T_c, which is evidenced by the smaller *n* value at higher T_c. This observation is consistent with the literature report.[69]

The crystallization half-life $t_{1/2}$ is defined as the time at which the extent of crystallization is complete 50%. Thus, $t_{1/2}$ can be experimentally determined when $X_{t_{1/2}}$= 0.5. It can also be calculated theoretically using Avrami exponent n and Avrami rate constant k as shown as following:

$$t_{1/2} = \left(\frac{\ln 2}{k}\right)^{1/n} \tag{3.6}$$
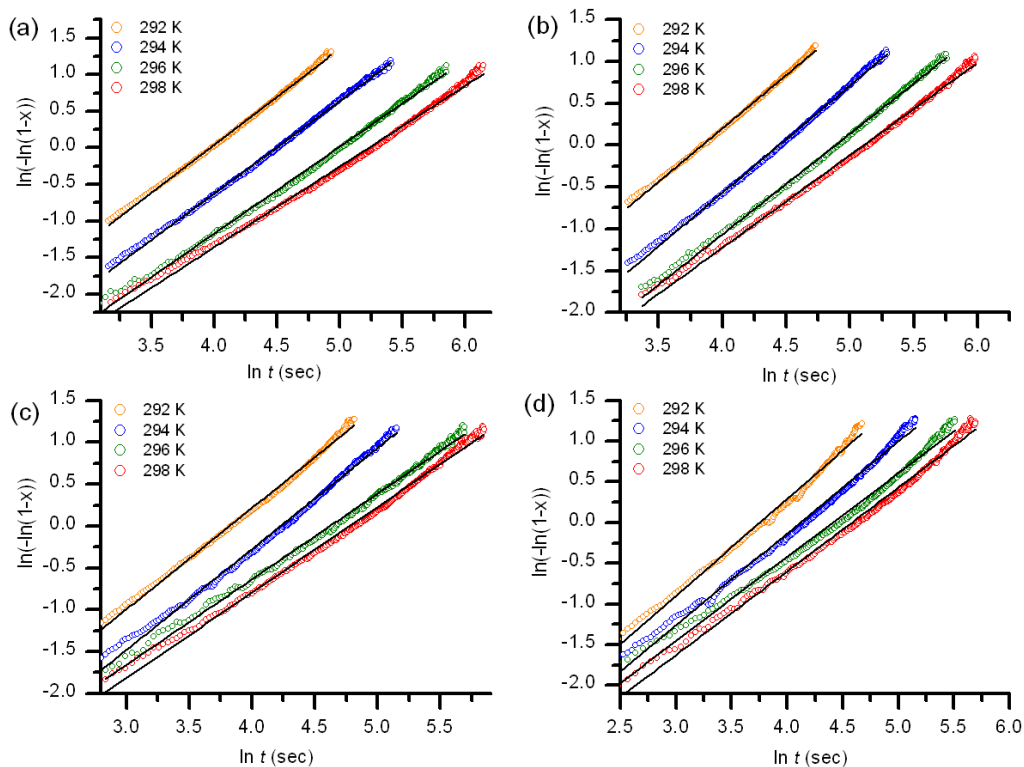
Figure 28. Plots of ln(-ln(1 - X_t)) versus ln t for isothermal crystallization of P3HT with various loading of SWNTs. (a) control P3HT (b) 0.10wt%, (c) 0.20wt% and (d) 0.30 wt%. Polymer concentration is 0.020 mg/mL.

Both experimental and theoretical $t_{1/2}$ are shown in Table 2. It shows that $t_{1/2,exp}$ and $t_{1/2, cal}$ are consistent with each other and it is obvious to observe that value of $t_{1/2}$ decreases with decreasing T_c. This is because a lower T_c leads to a higher supercooling degree, resulting in a faster formation of nuclei for crystallization. During isothermal condition, addition of SWNTs also decreases the value of $t_{1/2}$ because it increases the nucleation rate. This phenomenon is contributed to the fact that SWNTs perform as a heterogeneous nucleation agent to promote P3HT crystallization process.[65]

Table 2. Data of crystallization kinetics of P3HT with various loading of SWNTs in anisole at different crystallization temperature (T_c) from the rate law and the Avrami model

Sample designation	T_c [K]	Initial rate [s^{-1}] x 10^4	Reaction order α	Avrami exponent n	Avrami constant k x 10^3	$t_{1/2,exp}$ [s]	$t_{1/2,cal}$ [s]
Control P3HT	292	22.9	1.61	1.31	5.46	35.0	40.3
	294	10.9	1.64	1.27	3.38	68.5	66.1
	296	4.72	1.53	1.19	2.69	111.0	106
	298	2.77	1.69	1.10	3.09	140.0	137
0.10wt%SWNT	292	25.1	1.62	1.27	7.45	34.5	35.5
	294	11.4	1.72	1.27	3.38	65.0	66.1
	296	6.42	1.68	1.20	2.80	101.0	98.8
	298	4.52	1.84	1.11	3.52	123.0	117
0.20wt SWNT	292	26.8	1.59	1.21	9.76	34.0	33.9
	294	17.3	1.57	1.20	6.10	53.0	51.6
	296	9.03	1.68	1.02	8.83	75.0	72.1
	298	6.79	1.81	1.01	7.52	88.0	88.1
0.30wt%SWNT	292	25.8	1.69	1.19	11.3	33	31.8
	294	16.6	1.68	1.13	9.66	46.5	43.9
	296	10.7	1.86	1.03	10.6	61.0	57.9
	298	10.3	1.81	1.03	8.92	71.0	68.5

3.5 Chain-Folding

One of major characteristics for polymer crystallization process is chain folding and the fold surface free energy, σ_e, is determinative to chain folding during nucleation process.[55] Based on Hoffman-Lauritzen theory of secondary nucleation during chain-folding process,[60] the growth rate is determined by:

$$G = G_0 exp\left(\frac{-U^*}{R(T_c-T_\infty)}\right) exp\left(\frac{-K_g}{T_c\Delta T}\right) \qquad (3.7)$$

The first exponential term in equation above is associated with the diffusion process of the polymer chain segments in solution whereas the second exponential term represents the thermodynamic driving force of chain-folding during the nucleation process. In the diluted solution crystallization, the second exponential term is predominant over the first one.[47] In this case, the growth rate (G) of the crystals mainly depends on $1/T_c\Delta T$. HL theory is simplified and expressed by the equation below.

$$\ln G = \frac{-K_g}{T_c\Delta T} + A \qquad (3.8)$$

Figure 29a displays the plots of $\ln G$ versus $1/T_c\Delta T$ of the control P3HT with different concentrations. The best-fit straight line was found for each sample. From the slopes of the straight lines, the value of K_g of the control P3HT was determined to be about $1.20\times 10^6 K^2$. It is found that the K_g value is independent of the P3HT concentration in the range of 0.005 ~ 0.025 mg/mL. Therefore, the fold surface free energy σ_e remains constant in the diluted solution.
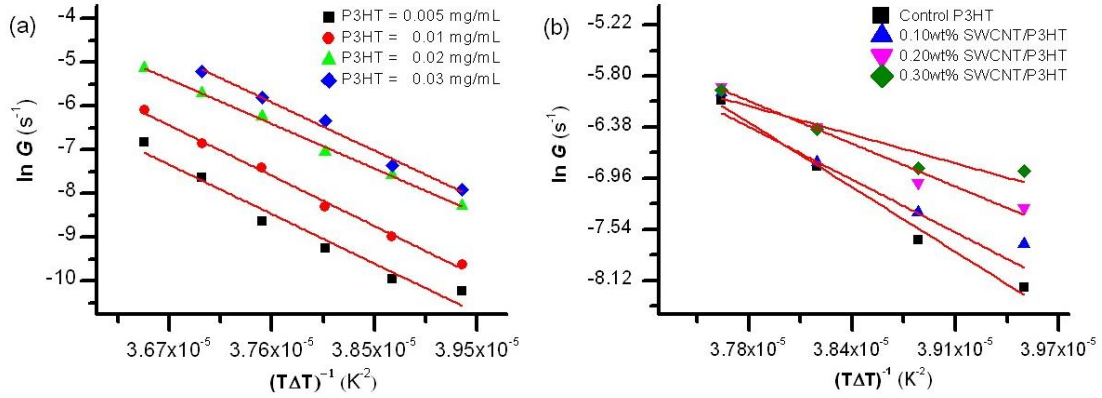
Figure 29. Plots of ln G versus $1/T\Delta T$. (a) the control P3HT with different polymer concentration and (b) P3HT with various loading of SWNTs. The P3HT concentration in (b) is 0.020mg/mL

However, addition of SWNTs to P3HT solution significantly decreases the K_g and thus the fold surface free energy σ_e. Figure 29b shows a plot of ln$G$ versus $1/T_c\Delta T$ of P3HT with various SWNT loading at P3HT concentration of 0.020 mg/mL. With increasing SWNT loading from 0.00wt% to 0.30wt%, K_g decreases from 1.16×10^6 to $0.512\times 10^6 K^2$. It has been reported that for P3HT crystals, $b = 7.75 \times 10^{-10}$m, $\sigma = 1.24\times 10^{-2}$Jm^{-2}, and $\Delta H_f = 1.096\times 10^8$Jm^{-3}.[69] From these values and Kg relationship with surface free folding energy, the value of $\sigma\sigma_e$ was calculated and thus, the value of σ_e was determined for each sample. The data is listed in Table 3. The data of the σ_e versus SWNT loading is plotted in Figure 30. The linear dependence is found.
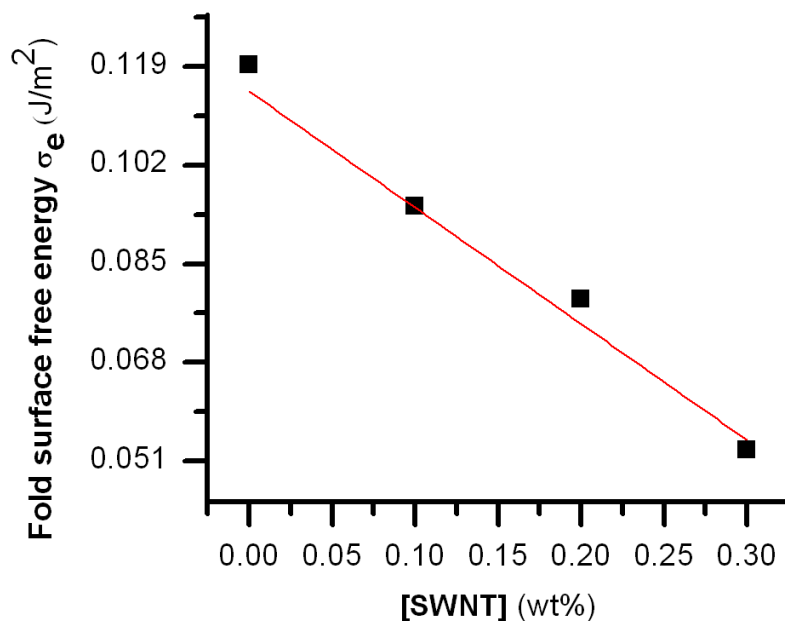
Figure 30. Fold surface free energy versus SWNT loading for solution

crystallization of P3HT in anisole. The P3HT concentration is 0.020mg/mL

The σ_e value of the control P3HT in anisole is ~ 0.119J/m², which is consistent

with our recent report on 0.103J/m² of P3HT in anisole.[48] Addition of only 0.30wt%

SWNTs to P3HT solution remarkably lowers the fold surface free energy σ_e by

55.4%. Such a significant change in the fold surface free energy of P3HT is

attributed to the effective interfacial interactions between P3HT and SWNTs.[43-45,65] It is believed that the lowering of the fold surface free energy is one of the

driving forces to accelerate P3HT crystallization in the solution containing

SWNTs. This thermodynamic analysis is consistent with our observations on the

crystallization kinetics from the reaction rate law and the nucleation mechanism

from the Avrami model.

Table 3. Data of thermodynamic characteristics of P3HT crystallization in the presence of SWNTs from Lauritzen-Hoffman model

Material	K_g [K^2] x10^{-6}	$\sigma \cdot \sigma_e$ [J^2 m^{-4}] x10^3	σ_e [J m^{-2}]
Control P3HT	1.16	1.48	0.119
0.10 wt% SWNTs/P3HT	0.925	1.17	0.0940
0.20 wt% SWNTs/P3HT	0.768	0.976	0.0787
0.30 wt% SWNTs/P3HT	0.515	0.655	0.0528

3.6 Characterization of GO

X-Ray Diffraction (XRD) measurement is an effective way to determine the atomic and molecular structure of crystals. Due to the structural differences, the incident X-rays is diffraction into different directions and diffraction angles. XRD result for the dry GO film on a glass slide shown in Figure 31 is consistent with literature data with ~10.2° diffraction peak corresponding to interlayer spacing of 0.85 nm. [52,71] Besides quantifying the interlayer spacing of exfoliated GO, Fourier transform infrared spectroscopy (FT-IR) is also used to verify the functional group attachments on oxidized exfoliated graphene sheets. FT-IR spectrum on Figure 32 shows the covalent vibration bands of C=O and aromatic stretch of C=C at 1719.34cm^{-1} and 1618.24cm^{-1} respectively. In addition, it's obvious to observe the strong OH stretch band at 3377.01cm^{-1} as well. XRD and FT-IR data verify the exfoliation and oxidized graphene nanosheets.
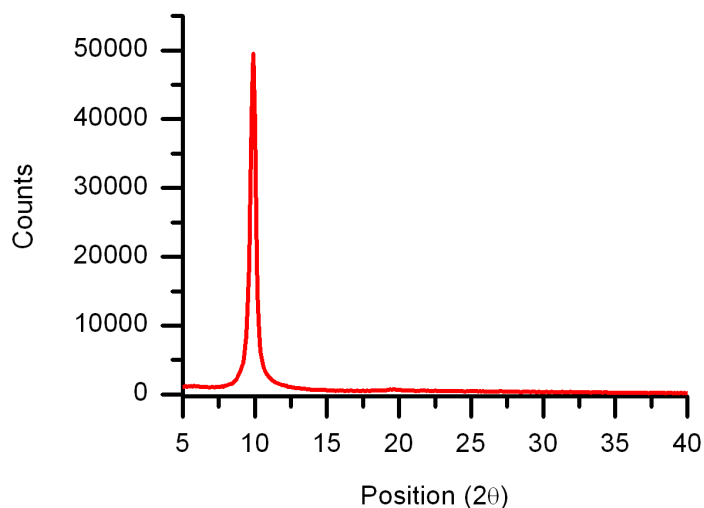
Figure 31. X-Ray diffraction pattern of exfoliated GO dry film

Atomic force microscope (AFM) is used to measure the dimensions and thickness of monolayer GO, and the size distribution of it. The difficulty in this measurement is the sample preparation. The reason is if the sample is too concentrated, it is challenge to image a location with one layer of GO only, so does the dilute sample. To see a monolayer of GO, we use both drop casting and spin coating methods on a clean and flat silicon substrate. The concentration of GO in this sample preparation is 0.1 mg/mL in ethanol. AFM image of monolayer GO as shown in Figure 33, the layer of GO is not perfect and it has defects on both edges and center. We believe this is due to the long oxidation time. The irregular shape and dimension of GO nanosheets are randomly distributed in the entire GO sample. The dimension of the showing AFM GO sheet is about 5 μm and the thickness of it is around 1 nm.
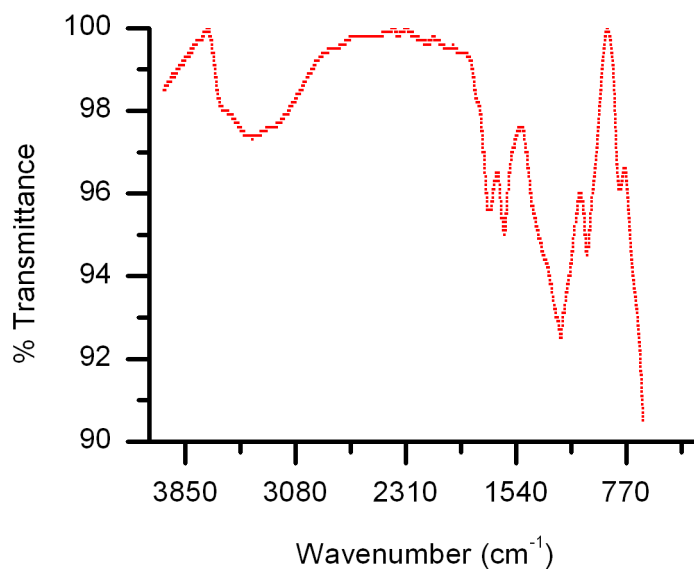
Figure 32. FTIR spectrum of GO dry film
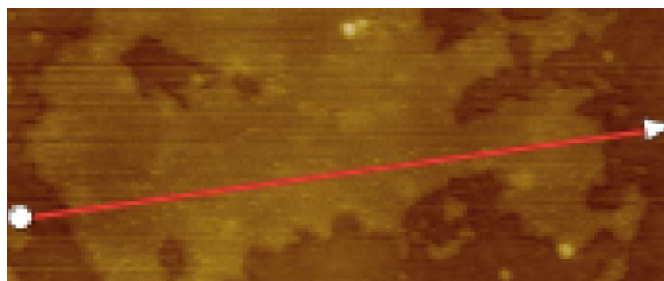
Figure 33. AFM image of monolayer GO. The length of this red line is around 5

$\mu m.$

3.7 Reduced Graphene Oxide-P3HT Solution Crystallization

Recently, several research groups have shown high-resolution morphology images of P3HT nanofibrils on a surface of two-dimensional graphene sheet.[52,72] According those nanofibrils formation, it is believed that graphene and P3HT do have strong interfacial interactions. In this work, we

conducted similar solution crystallization study of P3HT with the presence of reduced graphene (rGO) nanosheets. However, a set of non-consistent data is obtained with the addition of rGO dispersion in P3HT solution. Different solvents have been used to improve the solubility of either GO or rGO such as dichlorobenzene and anisole. No improvement has been observed for P3HT solution crystallization until the use of rGO in dimethylformamide (DMF). This preliminary study indicates that DMF is a great solvent in investigating rGO induced P3HT crystal formation and lots of future work need to make to improve rGO solubility in solution.

4. Conclusions

In summary, we have studied the kinetic behavior of isothermal solution crystallization of poly(3-hexylthiophene) in anisole in the presence of single-walled carbon nanotubes. Nanotubes serve as an orientation template and heterogeneous nucleation agent for polymer crystallization. The polymer forms crystalline nanofibrils perpendicular to the long axis of nanotubes. A detailed investigation on the crystallization kinetics shows that the system follows a complex rate law with a mixed fractional order. The secondary nucleation model displays predominant rod-rod aggregations. The Avrami analysis shows that polymer crystallization occurs by one-dimensional heterogeneous nucleation with linear growth. The chain-folding process is analyzed using the HL theory. It is evidenced that the addition of 0.3wt% SWNTs remarkably reduces the fold surface free energy. The study of kinetic behavior of isothermal solution crystallization of P3HT in anisole with the presence of reduced graphene oxide is unsuccessfully due to low solution processability of reduced graphene oxide in organic solvents.

5. Future Work

According to the UV-vis spectra, it shows DMF is one of the good solvent candidates to study P3HT solution crystallization process in the presence of rGO. To precisely evaluate the change of fold surface free energy in pure P3HT and P3HT-rGO systems, more research works need to be done in different isothermal temperatures. In additional, introducing surfactant molecules and conjugated polymer are the two possible approaches to improve rGO solubility and stability in solution, and prevention the formation of rGO aggregates.
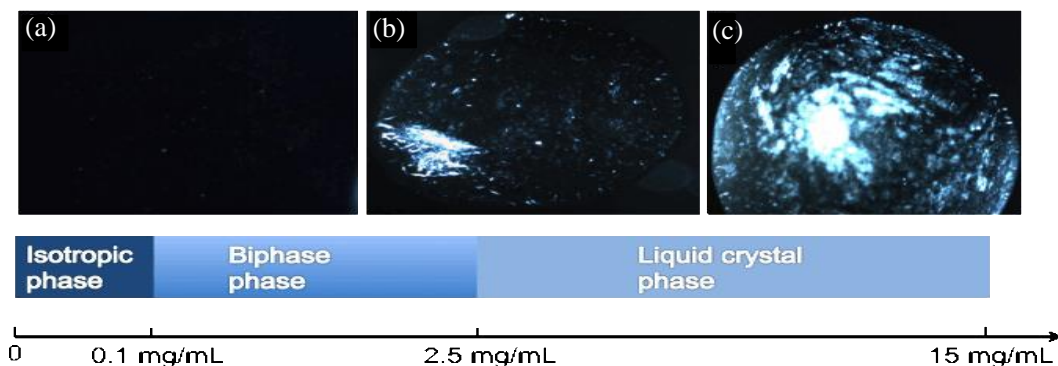
Figure 34. Phase diagram of GO. (a) Isotropic phase (b) Biphase (c) Liquid crystal phase

Even though no conclusion is made for P3HT-reduce graphene oxide solution crystallization process study, some other interesting properties of graphene oxide (GO) has been observed. Liquid crystal behavior of GO is one of them. GO has been reported to have liquid crystal phases recently.[73] It is believed that GO behaves as rod-like lyotropic liquid crystals. Phase transition of lyotropic liquid crystals is a function of both temperature and concentration. A

61

phase diagram or phase transition boundary of graphene oxide is evaluated by polarized optical microscope with varying GO concentration under isothermal condition as shown in Figure 34.

In addition to phase transition study, we surprisingly found different liquid crystal patterns of GO as shown on Figure 35. We believe the pattern variations are due to the alignment of GO nanosheets and the possible orientation alignment models that we propose are shown in Figure 36. In Figure 36b, GO nanosheets start to fold along the direction of flow or shear when the external force is not too strong. On the other hand, GO nanosheets have the tendency to move along flow direction if the flow rate is fast. Both models are used to further understand the alignment of GO and alter the sheet-alignment.
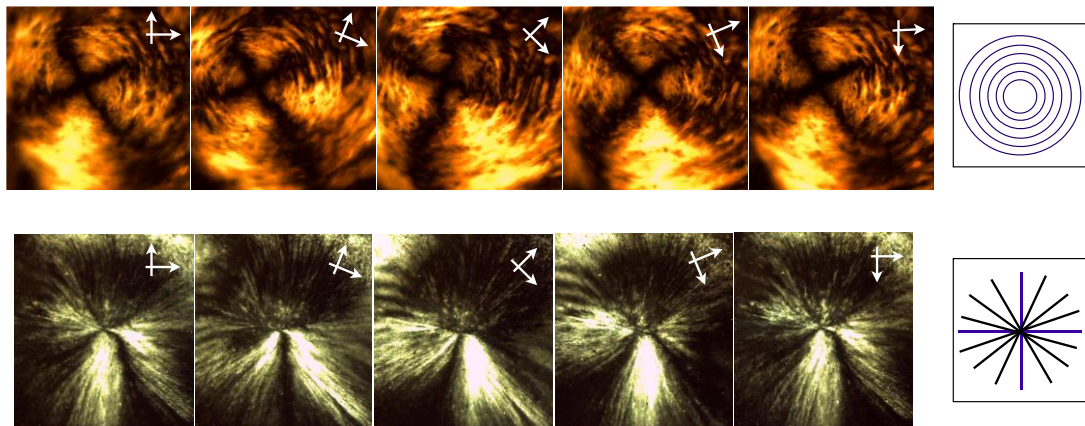
Figure 35. Two different GO liquid crystal patterns with 5 different rotations
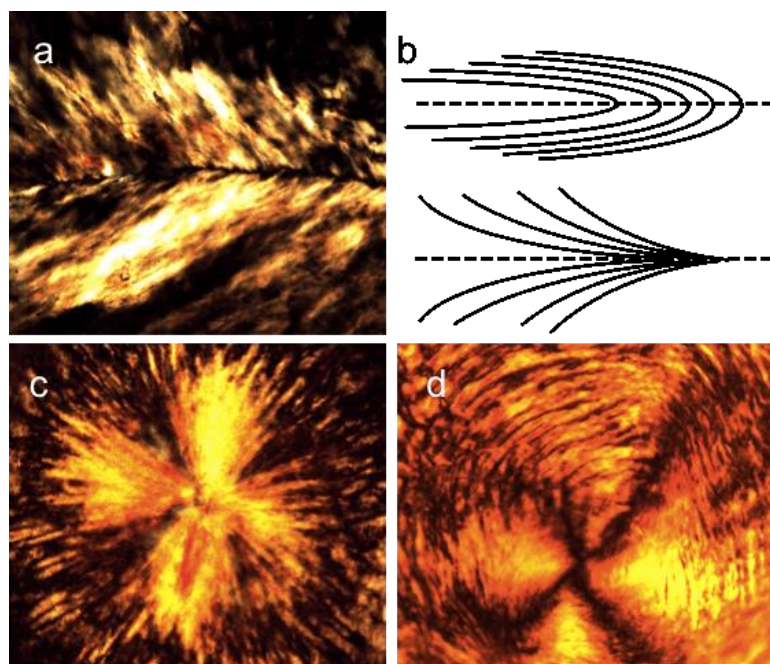
Figure 36. Predict models for GO alignments

To precisely verify these two models, we exploit microfluidic channels and use syringe pumps to control the fluid flow rate. Within the confined channel size, it is expected to see the transition between these two models by controlling the flow rate. Within the microfluidic channel, two different flow models are observed when controlling the flow rate (Figure 37). We believe different channel widths may have strong influence on the transitional flow rate, when GO nanosheets change their moving orientation. Thus, to determine channel width effect on transition flow rate of GO orientation is one of the objectives in the future.

Besides investigating the behavior of GO alignment and mobile orientation in the liquid crystal phase, evaluating the properties of GO fibers (Figure 38) and thin films is another goal. GO fibers are successfully made in calcium coagulation

bath and the GO thin film (35 μm) can be detach from Teflon substrate after the thin film formation.
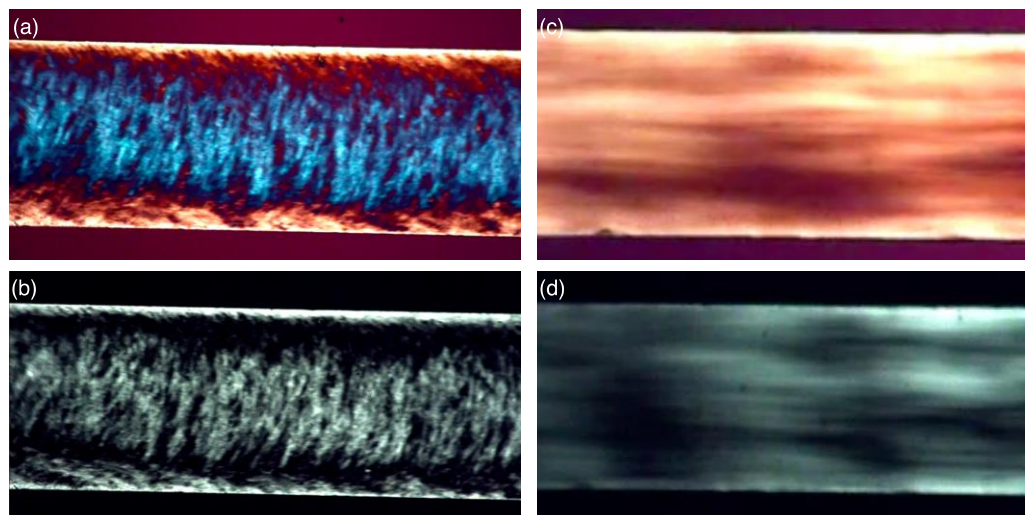
Figure 37. GO Nanosheets Orientation within 200 μm Microfluidic Channel. (a) and (b) have flow rate in 0.01 mL/hr; (c) and (d) have flow rate in 0.3 mL/hr
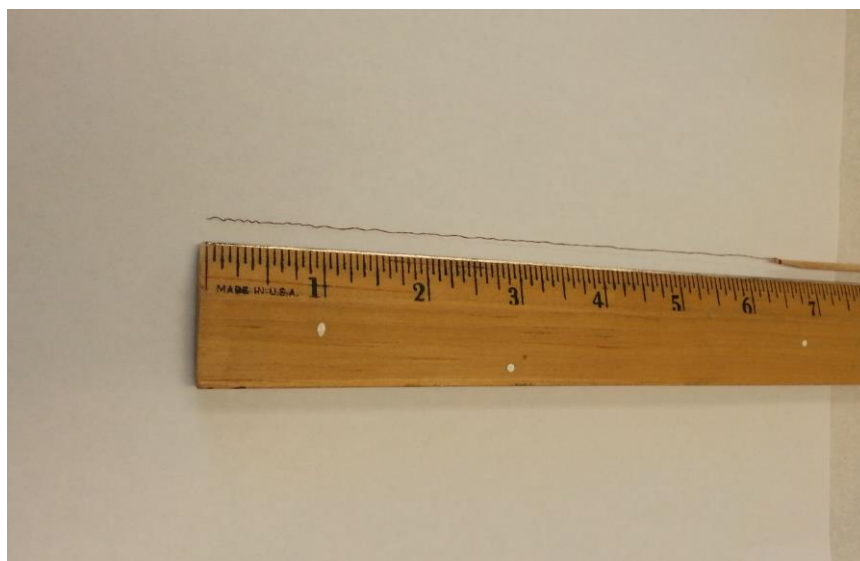
Figure 38. Illustration of GO Fiber

REFERENCES

1.   Chu, T.-Y. *et al.* Bulk heterojunction solar cells using thieno[3,4-c]pyrrole-4,6-dione and dithieno[3,2-b:2',3'-d]silole copolymer with a power conversion efficiency of 7.3%. *J. Am. Chem. Soc.* **133**, 4250–4253 (2011).

2.   Rahaman, M. & Tsuji, H. Isothermal crystallization and spherulite growth behavior of stereo multiblock poly (lactic acid) s: Effects of block length. *J. Appl. Polym. Sci.* **129**, 2502–2517 (2013).

3.   Chen, H.-C. *et al.* Prominent Short-Circuit Currents of Fluorinated Quinoxaline-Based Copolymer Solar Cells with a Power Conversion Efficiency of 8.0%. *Chemistry of Materials* 4766–4772 (2012).doi:10.1021/cm302861s&iName=master.img-000.jpg&w=190&h=134

4.   Bounioux, C., Katz, E. A. & Yerushalmi Rozen, R. Conjugated polymers‐ carbon nanotubes‐ based functional materials for organic photovoltaics: a critical review. *Polym. Adv. Technol.* **23**, 1129–1140 (2012).

5.   Price, S. C., Stuart, A. C., Yang, L., Zhou, H. & You, W. Fluorine substituted conjugated polymer of medium band gap yields 7% efficiency in polymer-fullerene solar cells. *J. Am. Chem. Soc.* **133**, 4625–4631 (2011).

6.   Zhou, H. *et al.* Development of fluorinated benzothiadiazole as a structural unit for a polymer solar cell of 7 % efficiency. *Angew. Chem.*

65

Int. Ed. Engl. **50**, 2995–2998 (2011).

7.   van Bavel, S., Veenstra, S. & Loos, J. On the importance of morphology control in polymer solar cells. *Macromol. Rapid Commun.* **31**, 1835–1845 (2010).

8.   Cataldo, S., Salice, P., Menna, E. & Pignataro, B. Carbon nanotubes and organic solar cells. *Energy Environ. Sci.* **5**, 5919–5940 (2012).

9.   Gomulya, W., Gao, J. & Loi, M. A. Conjugated polymer-wrapped carbon nanotubes: physical properties and device applications. *Eur. Phys. J. B* **86**, 404–401 (2013).

10.   Chiang, C. K. *et al.* Electrical conductivity in doped polyacetylene. *Physical Review Letters* **39**, 1098 (1977).

11.   Shirakawa, H., Louis, E. J., MacDiarmid, A. G., Chiang, C. K. & Heeger, A. J. Synthesis of electrically conducting organic polymers: halogen derivatives of polyacetylene, (CH) x. *J. Chem. Soc., Chem. Commun.* 578 (1977).doi:10.1039/c39770000578

12.   Nalwa, H. S. *Handbook of Advanced Electronic and Photonic Materials and Devices.* **8**, (Academic Press: 2000).

13.   Allen, N. S. *Handbook of Photochemistry and Photophysics of Polymeric Materials.* 1–707 (John Wiley & Sons : Hoboken, NJ, USA, 2010).

14.   Brinkmann, M. Structure and morphology control in thin films of regioregular poly (3- hexylthiophene). *J. Polym. Sci. B Polym. Phys.* **49**, 1218–1233 (2011).

15. Sirringhaus, H. *et al.* Two-dimensional charge transport in self-organized, high-mobility conjugated polymers. *Nature* **401**, 685–688 (1999).

16. Crossland, E. J. W., Rahimi, K., Reiter, G., Steiner, U. & Ludwigs, S. Systematic Control of Nucleation Density in Poly(3-Hexylthiophene) Thin Films. *Adv. Funct. Mater.* **21**, 518–524 (2010).

17. Wunderlich, B. & Grebowicz, J. Thermotropic mesophases and mesophase transitions of linear, flexible macromolecules. 1–59 (1984).

18. Heffner, G. W. & Pearson, D. S. Molecular characterization of poly (3-hexylthiophene). *Macromolecules* **24**, 6295–6299 (1991).

19. Jaczewska, J. *et al.* Swelling of poly (3-alkylthiophene) films exposed to solvent vapors and humidity: Evaluation of solubility parameters. *Synthetic Metals* **157**, 726–732 (2007).

20. Chen, C.-Y. *et al.* Formation and thermally-induced disruption of nanowhiskers in poly (3-hexylthiophene)/xylene gel studied by small-angle x-ray scattering. *Macromolecules* **43**, 7305–7311 (2010).

21. Brinkmann, M. & Rannou, P. Molecular Weight Dependence of Chain Packing and Semicrystalline Structure in Oriented Films of Regioregular Poly(3-hexylthiophene) Revealed by High-Resolution Transmission Electron Microscopy. *Macromolecules* **42**, 1125–1130 (2009).

22. Guo, Y., Han, Y. & Su, Z. Ordering of poly(3-hexylthiophene) in

solution and on substrates induced by concentrated sulfuric acid. *J. Phys. Chem. B* **117**, 14842–14848 (2013).

23.   Chang, J.-F. *et al.* Enhanced Mobility of Poly(3-hexylthiophene) Transistors by Spin-Coating from High-Boiling-Point Solvents. *Chemistry of Materials* **16**, 4772–4776 (2004).

24.   Stranks, S. D., Habisreutinger, S. N., Dirks, B. & Nicholas, R. J. Novel Carbon Nanotube‐ Conjugated Polymer Nanohybrids Produced By Multiple Polymer Processing. *Adv. Mater.* **25**, 4365–4371 (2013).

25.   Danesh, C. D., Starkweather, N. S. & Zhang, S. In situ study of dynamic conformational transitions of a water-soluble poly(3-hexylthiophene) derivative by surfactant complexation. *J. Phys. Chem. B* **116**, 12887–12894 (2012).

26.   Kwon, T., Lee, G., Choi, H., Strano, M. S. & Kim, W.-J. Highly efficient exfoliation of individual single-walled carbon nanotubes by biocompatible phenoxylated dextran. *Nanoscale* **5**, 6773–6778 (2013).

27.   Gregg, B. A. & Hanna, M. C. Comparing organic to inorganic photovoltaic cells: Theory, experiment, and simulation. *J. Appl. Phys.* **93**, 3605 (2003).

28.   Ratier, B., Nunzi, J.-M., Aldissi, M., Kraft, T. M. & Buncel, E. Organic solar cell materials and active layer designs—improvements with carbon nanotubes: a review. *Polym. Int.* **61**, 342–354 (2012).

29.   Lu, R., Christianson, C., Kirkeminde, A., Ren, S. & Wu, J. Extraordinary photocurrent harvesting at type-II heterojunction

interfaces: toward high detectivity carbon nanotube infrared detectors. *Nano Lett.* **12**, 6244–6249 (2012).

30.   Minnaert, B. & Burgelman, M. Efficiency potential of organic bulk heterojunction solar cells. *Prog. Photovolt: Res. Appl.* **15**, 741–748 (2007).

31.   Ham Evidence for high-efficiency exciton dissociation at polymer/single-walled carbon nanotube interfaces in planar nano-heterojunction photovoltaics. *ACS Nano* **4**, 6251–6259 (2010).

32.   Ren, S. *et al.* Toward efficient carbon nanotube/P3HT solar cells: active layer morphology, electrical, and optical properties. *Nano Lett.* **11**, 5316–5321 (2011).

33.   Matsuda, Y., Tahir-Kheli, J. & Goddard, W. A., III Definitive Band Gaps for Single-Wall Carbon Nanotubes. *J. Phys. Chem. Lett.* **1**, 2946–2950 (2010).

34.   Lee, J. M. *et al.* Selective Electron- or Hole- Transport Enhancement in Bulk- Heterojunction Organic Solar Cells with N- or B- Doped Carbon Nanotubes. *Adv. Mater.* **23**, 629–633 (2011).

35.   Kymakis, E., Koudoumas, E., Franghiadakis, I. & Amaratunga, G. A. J. Post-fabrication annealing effects in polymer-nanotube photovoltaic cells. *J. Phys. D: Appl. Phys.* **39**, 1058–1062 (2006).

36.   Ding, J., Yan, X. & Cao, J. Analytical relation of band gaps to both chirality and diameter of single-wall carbon nanotubes. *Phys. Rev. B* **66**, 073401 (2002).

37.   Lee, H. W. *et al.* Selective dispersion of high purity semiconducting single-walled carbon nanotubes with regioregular poly(3-alkylthiophene)s. *Nature Communications* **2**, 541–8 (2011).

38.   Nish, A., Hwang, J.-Y., Doig, J. & Nicholas, R. J. Highly selective dispersion of single-walled carbon nanotubes using aromatic polymers. *Nature Nanotech* **2**, 640–646 (2007).

39.   Kang, Y. K. *et al.* Helical wrapping of single-walled carbon nanotubes by water soluble poly(p-phenyleneethynylene). *Nano Lett.* **9**, 1414–1418 (2009).

40.   Deria, P. *et al.* Single-handed helical wrapping of single-walled carbon nanotubes by chiral, ionic, semiconducting polymers. *J. Am. Chem. Soc.* **135**, 16220–16234 (2013).

41.   Caddeo, C., Melis, C., Colombo, L. & Mattoni, A. Understanding the helical wrapping of poly (3-hexylthiophene) on carbon nanotubes. *J. Phys. Chem. C* **114**, 21109–21113 (2010).

42.   Li, L., Li, C. Y. & Ni, C. Polymer crystallization-driven, periodic patterning on carbon nanotubes. *J. Am. Chem. Soc.* **128**, 1692–1699 (2006).

43.   Bernardi, M., Giulianini, M. & Grossman, J. C. Self-assembly and its impact on interfacial charge transfer in carbon nanotube/P3HT solar cells. *ACS Nano* **4**, 6599–6606 (2010).

44.   Yang, M., Koutsos, V. & Zaiser, M. Interactions between polymers and carbon nanotubes: a molecular dynamics study. *J. Phys. Chem.*

B **109**, 10009–10014 (2005).

45.   Guo, R., Tan, Z., Xu, K. & Yan, L.-T. Length-Dependent Assembly of

a Stiff Polymer Chain at the Interface of a Carbon Nanotube

. *ACS macro Letters* 977–981

(2012).doi:10.1021/mz300221s&iName=master.img-

000.jpg&w=238&h=133

46.   Holt, J. M. *et al.* Prolonging Charge Separation in P3HT− SWNT

Composites Using Highly Enriched Semiconducting Nanotubes. *Nano

Lett.* **10**, 4627–4633 (2010).

47.   Zhang, S. *et al.* Surface-Induced Polymer Crystallization in High

Volume Fraction Aligned Carbon Nanotube-Polymer Composites.

Macromol. Chem. Phys. **9999**, NA–NA (2010).

48.   Wagner, T. W., Luo, Y., Redeker, N. D., Immoos, C. E. & Zhang, S.

Effect of surface-modified zinc oxide nanowires on solution

crystallization kinetics of poly (3-hexylthiophene). *Polymer* **55**, 2008–

2013 (2014).

49.   Dias, Y. & Yerushalmi Rozen, R. Entropic effects in carbon

nanotubes-templated crystallization of Poly(3-alkyl thiophenes, P3HT,

P3OT). *Polymer* **54**, 6399–6405 (2013).

50.   Huang, G. *et al.* Highly Strong and Elastic Graphene Fibres Prepared

from Universal Graphene Oxide Precursors. *Sci. Rep.* **4**, (2014).

51.   Joshi, R. K. *et al.* Precise and Ultrafast Molecular Sieving Through

Graphene Oxide Membranes. *Science* **343**, 752–754 (2014).

52.   Chunder, A., Liu, J. & Zhai, L. Reduced Graphene Oxide/Poly(3-hexylthiophene) Supramolecular Composites. *Macromol. Rapid Commun.* **31**, 380–384 (2010).

53.   Tung, V. C. *et al.* Low-Temperature Solution Processing of Graphene−Carbon Nanotube Hybrid Materials for High-Performance Transparent Conductors. *Nano Lett.* **9**, 1949–1955 (2009).

54.   Li, S.-S., Tu, K.-H., Lin, C.-C., Chen, C.-W. & Chhowalla, M. Solution-Processable Graphene Oxide as an Efficient Hole Transport Layer in Polymer Solar Cells. *ACS Nano* **4**, 3169–3174 (2010).

55.   Cheng, S. Z. & Lotz, B. Enthalpic and entropic origins of nucleation barriers during polymer crystallization: the Hoffman–Lauritzen theory and beyond. *Polymer* **46**, 8662–8681 (2005).

56.   Avrami, M. Kinetics of Phase Change. I General Theory. *J. Chem. Phys.* **7**, 1103 (1939).

57.   Ding, N. & Amis, E. J. Kinetics of poly (ethylene oxide) crystallization from solution: concentration dependence. *Macromolecules* **24**, 6464–6469 (1991).

58.   Cooper, M. & Manley, R. S. J. Growth Kinetics of Polyethylene Single Crystals. I. Growth of (110) Faces of Crystals from Dilute Solutions in Xylene. *Macromolecules* **8**, 219–227 (1975).

59.   Ratta, V. Crystallization, morphology, thermal stability and adhesive properties of novel high performance semicrystalline polyimides. (1999).

60.   Hoffman, J. D. & Miller, R. L. Kinetics of crystallization from the melt and chain folding in polyethylene fractions revisited: theory and experiment. *Polymer* **38**, 3151–3212

61.   Hummers, W. S., Jr & Offeman, R. E. Preparation of graphitic oxide. *J. Am. Chem. Soc.* **80**, 1339–1339 (1958).

62.   Harvey, D. *Modern Analytical Chemistry*. 1–124 (McGraw-Hill Companies: 2010).

63.   Li, B., Li, L., Wang, B. & Li, C. Y. Alternating patterns on single-walled carbon nanotubes. *Nature Nanotech* **4**, 358–362 (2009).

64.   Minus, M. L., Chae, H. G. & Kumar, S. Polyethylene crystallization nucleated by carbon nanotubes under shear. *ACS Appl. Mater. Interfaces* **4**, 326–330 (2012).

65.   Liu, J., Zou, J. & Zhai, L. Bottom-up Assembly of Poly(3-hexylthiophene) on Carbon Nanotubes: 2D Building Blocks for Nanoscale Circuits. *Macromol. Rapid Commun.* **30**, 1387–1391 (2009).

66.   Geng, J. & Zeng, T. Influence of single-walled carbon nanotubes induced crystallinity enhancement and morphology change on polymer photovoltaic devices. *J. Am. Chem. Soc.* **128**, 16827–16833 (2006).

67.   Scharsich, C. *et al.* Control of aggregate formation in poly (3- hexylthiophene) by solvent, molecular weight, and synthetic method. *J. Polym. Sci. B Polym. Phys.* **50**, 442–453 (2012).

68.   Gupta, A. & Choudhary, V. Isothermal crystallization kinetics of poly (trimethylene terephthalate)/multiwall carbon nanotubes composites. *J Therm Anal Calorim* **114**, 643–651 (2013).

69.   Malik, S. & Nandi, A. K. Crystallization mechanism of regioregular poly (3- alkyl thiophene) s. *J. Polym. Sci. B Polym. Phys.* **40**, 2073–2085 (2002).

70.   Liu, S. L. & Chung, T. S. Crystallization and melting behavior of regioregular poly (3-dodecylthiophene). *Polymer* **41**, 2781–2793 (2000).

71.   Wang, J. *et al.* Green synthesis of graphene nanosheets/ZnO composites and electrochemical properties. *Journal of Solid State Chemistry* **184**, 1421–1427 (2011).

72.   Yang, Z. & Lu, H. Nonisothermal crystallization behaviors of poly(3-hexylthiophene)/reduced graphene oxide nanocomposites. *J. Appl. Polym. Sci.* **128**, 802–810 (2012).

73.   Kim, J. E. *et al.* Graphene Oxide Liquid Crystals. *Angew. Chem. Int. Ed.* **50**, 3043–3047 (2011).